FU JEN STUDIES

NATURAL SCIENCES

NO. 18 1984

CONTENTS

FU JEN UNIVERSITY

TAIPEI, TAIWAN, REPUBLIC OF CHINA

ELECTRICAL AND MODULATION OPTICAL PROPERTIES OF 2H-$MoSe_2$

YING-SHENG HUANG

ABSTRACT

A "two-step" halogen vapor transport method has been developed for growing large size single crystals of $MoSe_2$ of 2H form. The electrical and modulation optical properties are investigated in order to get a better understanding of its band structure. Conductivity measurements show that intrinsic conductivity begins to dominate at 650 °K with a thermal energy gap around 1 eV. The optical properties are studied by thermoreflectance (TR) and electrolyte electroreflectance (EER) techniques in the range of 1.4 to 6.2 eV at room temperature. Both TR and EER spectra exhibit sharp structures in the vicinity of the excitonic transitions A, B, A′ and B′ as well as higher lying interband transitions. A comparison of TR and EER spectrum helps to identify the various features in the spectra of these two different modulated techniques. The interband transition energies are then determined with a better accuracy. The electrical and optical results confirm the band structure model proposed by Kasowski.

INTRODUCTION

Layered compounds of the transition-metal dichalcogenide have been the subject of intensive theoretical and experimental studies because of their possible application as high temperature superconductors[1], as solid superionic cathodes in new battery systems[2], as a new class of electrodes for photoelectrochemical cells[3]; and because of their unusual anisotropic physical properties.[4-5] $MoSe_2$ is a member of this family of compounds which has not been as extensively studied as MoS_2 because it is not as easily available.

$MoSe_2$ is a semiconducting compound. The structure of 2H-$MoSe_2$ has sixfold trigonal prismatic coordination of the Mo atoms by the Se stoms within the layers, and there are two layers per unit cell stacked in hexagonal symmetry. The structure belongs to the space D_{6h}^4. There is strong covalent bonding within the layers and a weak Van der Waal's force between the layers. As a consequence, there is significant asymmetry (by a factor of 10^2 to 10^3)

between the transport properties parallel and perpendicular to the layers. Crystals can be cleaved readily in very thin plates parallel to the layers perpendicular to the hexagonal *c*-axis.

Only relatively incomplete experimental information on its solid state properties have been reported. In addition very little theoretical data exist on the band structure of $MoSe_2$. There are several modulation spectroscopic methods[6-9] to study the excitions A, B, A′ and B′ in the range 1.4 to 3 eV but little is known about the higher energy features. A complete understanding of the band structure is not possible without a detailed study of the higher energy interband transitions.

A "two-step" halogen vapor transport method has been developed for growing large size single crystals of 2H-$MoSe_2$. The temperature dependence of conductivity has been studied between 135 °K and 800 °K by using a four probe potentiometric technique. Both thermoreflectance (TR) and electrolyte electroreflectance (EER) techniques have been employed to study the optical spectra of $MoSe_2$ in the range of 1.4 to 6.2 eV at room temperature. A comparison of TR and EER spectrum helps to identify the various features in the spectra of these two techniques. The interband transition energies are then determined with a better accuracy than that achieved in the past. This gives a better understanding of the band structure of 2H-$MoSe_2$.

EXPERIMENTAL TECHNIQUES

Crystal Growth

The crystals were grown by a two step halogen vapor transport method with Br_2 as the transporting agent. Small crystals were grown first from a stochiometric mixture of the powdered elements. The product of the first step became the starting material for the second growth which yielded crystals for study.

The starting materials together with the carrier substance were placed in a quartz ampoule (40 mm in diameter) which was then evacuated to a pressure about 10^{-6} torr and sealed. Crystal growth was conducted by inserting the filled ampoule in a horizontal tube

furnace in which the appropriate temperatures and thermal gradients had been established, and leaving it undisturbed for a period of two to three weeks.

The crystal growth apparatus is shown in Fig. 1a. It consists essentially of a gradient furnace that permits careful control of the temperatures and temperature gradients in the regions of reaction and growth. The high temperature was provided by a Lindberg 54259 three zone tube furnace with model 59495-A control console. A typical thermal gradient is shown in Fig. 1b. Monitoring the temperature indicated that fluctuations in temperature were less than 1% during the entire growing period. At the end of this period the ampoule was removed from the furnace and wet tissues were rapidly applied to the end away from the crystals to condense the Br_2 vapor. When the remainder of the ampoule had cooled to room temperature the ampoule was opened and the crystals which had grown at the cooler end were removed.

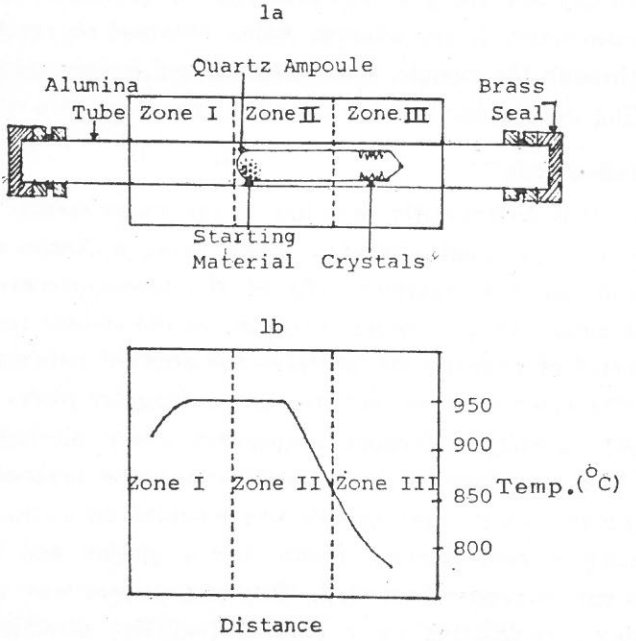

Fig. 1. Setup and temperature profile for the growth of $MoSe_2$ crystals.

Conductivity Measurements

The temperature dependence of conductivity of ten samples from two different batches was studied between 135 °K and 800 °K by using a four probe potentiometric technique.[10] The samples (thickness t) were cut into a rectangular shape of effective length l and width b. Electrical connections to the crystal were made by means of four parallel platinum wires laid across the basal susface of the thin crystal and attached to the crystal surface by means of conducting silver paint. The wires near each end of the rectangular crystal acted as current leads while the two contact wires (separation d) on either side of the centre line were used to measure the potential difference V in the crystal. With this electrode configuration the conductivity is σ defined by

$$\sigma = \frac{Id}{Vbt}$$

where I is the current through the sample from a constant current supply and the potential difference V, measured by a sensitive potentiometer, is the average value obtained on reversing the current through the sample. Dimensions d and b were measured by a travelling microscope and the crystal thickness t by a dial gauge.

Thermoreflectance[11]

Figure 2 is a schematic drawing of the experimental arrangement for the TR measurements. Light from a Xenon arc lamp is focused on the entrance slit of the monochromator. The emergent monochromatic beam is focused on the sample from which it is reflected at near-normal incidence and directed onto a photomultiplier. The samples were cut into thin rectangular pieces to reduce their heat capacity. Vacuum evaporated silver electrodes were applied to the surface of the crystals on a plane perpendicular to the hexagonal c-axis. The sample was mounted on a thin layer of mylar with silicone vacuum grease for insulation and then was attached onto a copper heat sink. The temperature was modulated by passing a modulating pulse current (~10 Hz) directly through the samples. The signal at the output of the photomultiplier

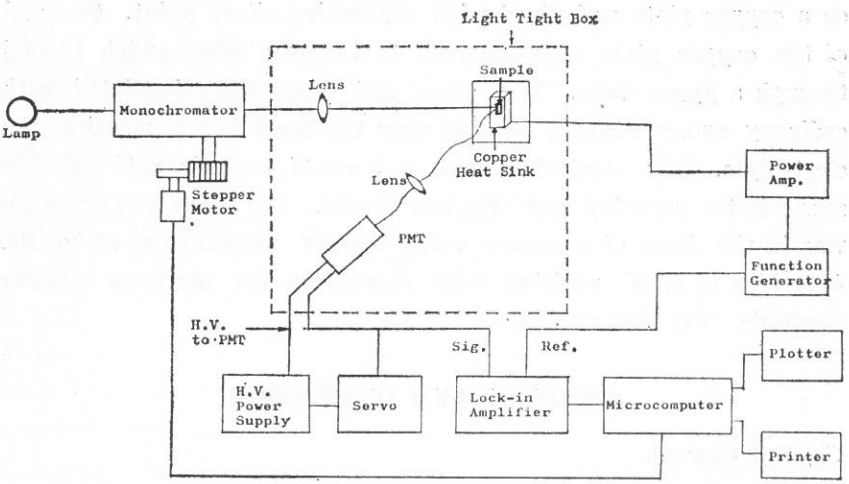

Fig. 2. Experimental arrangement for thermoreflectance.

contains two components: a *dc* part, $S = \gamma I_i R$, and a small *ac* component, $\Delta S = \gamma I_i \Delta R$ where γ is the sensitivity of the photomultiplier; I_i, the incident light intensity; R, the reflectivity of the sample and ΔR is the change in the reflectivity of the sample caused by the temperature modification. The quantity of interest is the relative reflectivity, $\Delta R/R$, which is related to the relative signal. It is apparent that

$$\frac{\Delta S}{S} = \frac{\gamma I_i \Delta R}{\gamma I_i R} = \frac{\Delta R}{R}$$

The *dc* output, S, is maintained constant throughout the experiment by a servomechanism which controls the high voltage applied to the photomultiplier. The *ac* component, ΔS, is detected by a lock-in amplifier. Under these conditions the output from the lock-in amplifier which goes to a microcomputer, is directly proportional to $\Delta R/R$.

Electrolyte Electroreflectance

The electrolyte electroreflectance (EER) technique has been described extensively in the literature.[12,13] The $MoSe_2$ electrode was prepared in the following way: The crystals were mounted

on a copper plate and glued with conducting silver paint. One end of the copper plate was soldered to a copper wire which passed through a pyrex tube. The wires and plate were insulated with ordinary epoxy cement, leaving only the basal face exposed to the electrolyte. The electrolyte was a 3 wt.% tartaric acid solution mixed in the ratio 1:2 with ethylene glycol. The modulating voltage was in the form of a square wave, 100 mV peak-to-peak at 100 Hz. A *dc* bias of 0.1 V, positive with respect to the platinum counter electrode, was also applied to the sample.

RESULTS AND DISCUSSION

Crystal Growth

The halogen gases are best suited as transporting agents for the chalcogenides.[14] We have employed Br_2 for the growth of $MoSe_2$ crystals. The chemical reaction is

$$MoSe_{2,\,s} + Br_{2,\,g} \rightleftarrows MoBr_{2,\,g} + Se_{2,\,g}$$

Crystals of $10\times10\times1\,mm^3$ with mirror-like surfaces are obtained on a routine basis. The success in growing large single crystals of $MoSe_2$ is based on the use of a two-step process, in which the initial step served to purify the starting materials. It also produces a more compact starting material. In the second step, the nucleation is less than in the original growth, and hence much larger crystals appeared. Crystals were grown in a variety of temperatures, temperature gradients and Br_2 concentrations. The optimum conditions are: The reaction temperature is about 960°C, the growth temperature is in the range of 840°C to 800°C, and the Br_2 concentation is $2\,mg/cm^3$. The crystal structure was studied by X-ray powder diffraction and was confirmed to have a 2H form.

Conductivity

Figure 3 shows measured values of conductivity, σ, over the temperature range 135 °K to 800 °K for two different samples of 2H-$MoSe_2$. The curve labeled (a), is for the sample grown from the constituent elements. The curve labeled (b), is for the sample

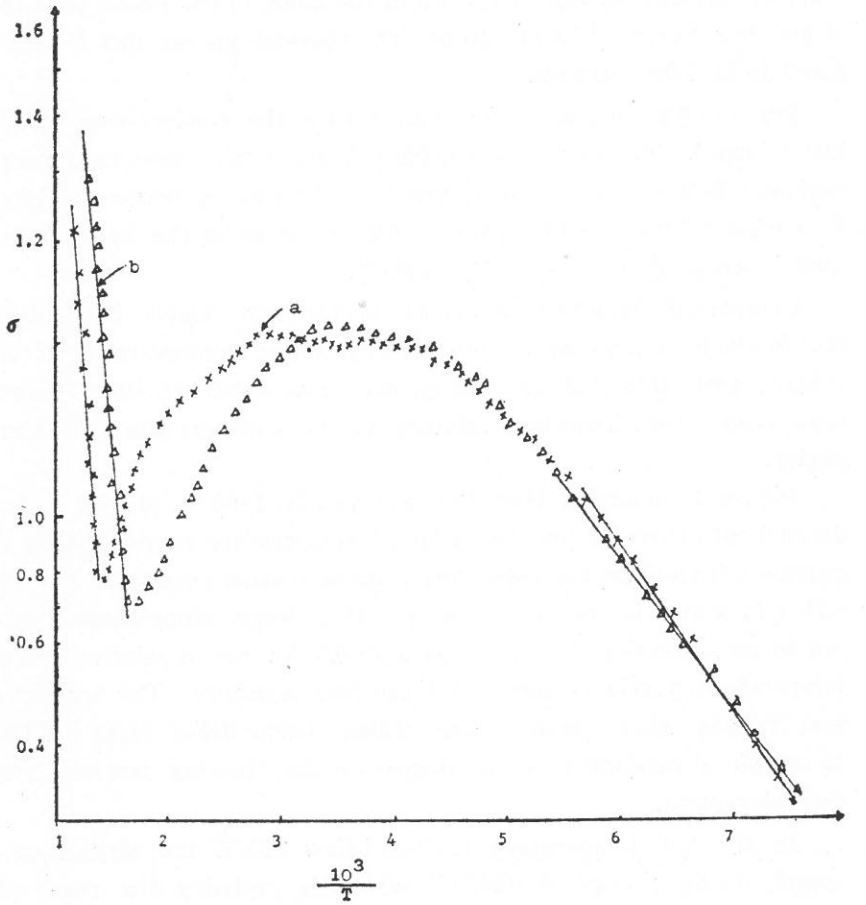

Fig. 3. Graph of σ ($\Omega^{-1}\,cm^{-1}$) versus $10^3/T$ for two different single crystals of n-$MoSe_2$.
(a) crystal grown from the constituent elements.
(b) crystal grown from small crystals.

grown from small crystals. Both crystals are n-type at room temperature.

For sample (a), at room temperature the conductivity, σ, is $1.08\,\Omega^{-1}\,cm^{-1}$. Curve (a) shows two linear regions. Below room temperature the thermal activation energy was 0.148 ± 0.04 eV. At temperatures above 700°K the electrical conductivity increases rapidly with rising temperature. This behavior is attributed to the

onset of intrinsic conductivity. From the slope of the linear portion of the $\ln\sigma$ versus 1,000/T graph, the thermal energy gap is computed to be 1.006 ± 0.04 eV.

For sample (b), at room temperature the conductivity, σ, is $1.02\,\Omega^{-1}\,cm^{-1}$. The $\ln\sigma$ versus 1,000/T graph again shows two linear regions. Below room temperature the thermal activation energy $E_a = 0.142 \pm 0.04$ eV while above 650°K the slope of the $\ln\sigma$ versus 1,000/T graph gives $E_t = 0.990 \pm 0.04$ eV.

Comparing these two curves we observe that sample (b) reaches the intrinsic region at a substantially lower temperature. It is evident from this that crystals grown from small crystals rather than from a stoichiometric mixture of the elements are of higher purity.

Figure 3 indicates that the $\ln\sigma$ versus 1,000/T plots can be divided into three segments: a "low" temperature region having a portion with a slope corresponding to an activation energy of around 0.145 eV; a high temperature region with a steeper slope corresponding to an activation energy of around 0.5 eV; and a relatively flat intermediate portion connecting these two segments. The temperature ranges where these various regions occur differ from sample to sample depending to some degree on the starting material for crystal growth.

In the low temperature region, below 200 °K the slope corresponds to an energy of 0.145 eV which is probably the result of impurity activation. Fivaz and Mooser,[15], observed a slope in this region corresponding to an energy of 0.16 eV which they associated with an extrinsic process, and El-Mahalawy and Evans[10] found a value of 0.14 eV which they suggest could be the result of intrinsic processes in the crystal.

Our observations in the high temperature region are similar to those of other investigators. Above 650 °K the $\ln\sigma$ vs 1,000/T curve yields a thermal band gap, $E_t = 1.0$ eV. Evans and Hazelwood[16] reported measurements on *n*-type $MoSe_2$ crystals grown directly from the vapor of $E_t = 1.1$ eV in the temperature range above 700°K, El-Mahalawy and Evans[10] reported 0.95 eV which they claimed

to represent the indirect band gap.

Thermoreflectance and Electrolyte Electroreflectance

The TR and EER spectra of $MoSe_2$ at room temperature in the range of 1.4 to 6.2 eV are shown in Fig. 4 and Fig. 5 respectively. The structures have been labelled according to the commonly used notation for the metal-dichalcogenide compounds. Both the TR and EER spectrum show sharp structures in the vicinity of the excitonic transitions A, B, A′ and B′ as well as higher lying interband transitions. It is well established that minima in TR spectra correspond to inflexion points in the reflectivity spectra[17] and thus can be related to maxima in the absorption spectra.[18] The EER spectrum contains features differing significantly in the structure from those of the TR spectrum, but which occur approximatedly at the same spectral locations. By the "three-point method"[19] we can determine the position of the interband transitions and the accuracy is better than ±5 meV. Table 1 shows the energy position from the TR and EER spectrum. The energy positions found by

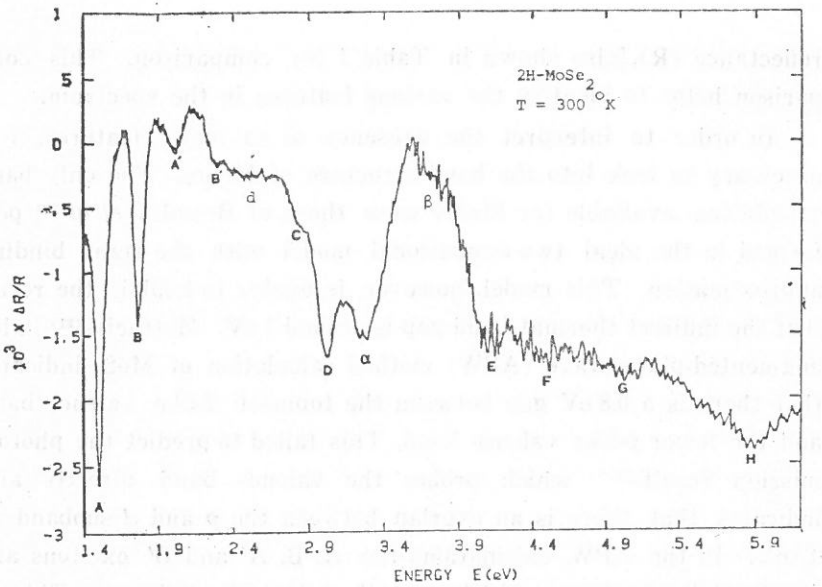

Fig. 4. The TR spectrum of 2H-$MoSe_2$ in the range of 1.4 to 6.2 eV.

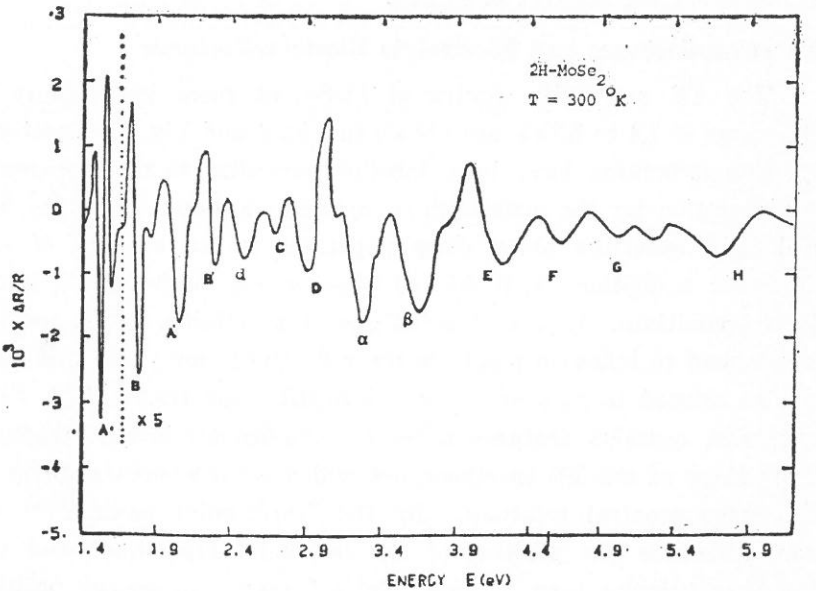

Fig. 5. The EER spectrum of 2H-$MoSe_2$ in the range of 1.4 to 6.2 eV with $E \perp c$.

reflectance (R), also shown in Table 1 for comparison. This comparison helps to identify the various features in the spectrum.

In order to interpret the presence of so many features, it is necessary to look into the band structure of $MoSe_2$. The only band calculation available for $MoSe_2$ were those of Bromley *et al*[20] performed in the ideal two-dimensional model with the tight binding approximation. This model, however, is unable to explain the result that the indirect thermal band gap is around 1 eV. Mattheiss[21] in his augmented-plane wave (APW) method calculation of MoS_2 indicates that there is a 0.8 eV gap between the topmost *d*-like valence band and the lower *p*-like valence band. This failed to predict the photoemission results[22] which probes the valence band directly and indicates that there is an overlap between the *p* and *d* subband at 0.5 eV. In the APW calculations the A, B, A′ and B′ excitons are due to *d-d* transitions which are allowed at the point Γ. This is contrary to the modulation results[7,8] which indicates that A, B

Table 1. A comparison of the energy positions of the various features in the TR, EER and R^{17} spectra

Feature	Energy (eV)		
	TR	EER	R^{17}
A	1.522	1.544	1.51
B	1.774	1.785	1.74
A′	2.028	2.062	2.05
B′	2.306	2.311	2.20
d	2.557	2.564	2.63
C	2.783	2.767	2.77
D	3.021	2.988	2.95
α	3.272	3.264	3.22
β	3.535	3.552	3.64
E	4.094	4.113	4.07
F	4.463	4.481	
G	5.057	5.102	
H	5.812	5.796	5.84

excitons and the A′, B′ excitons have different origins. On the other hand the linear combination of muffin-tin orbitals (LCMTO) calculations made by Kasowski[23] for MoS_2 and NbS_2 are in good agreement with experiments (absorption[18] and photoemission[22]). The two compounds belong to the same symmetry group D_{6h}^4 as $MoSe_2$. Therefore we choose to use the Kasowski model as a guide to determine the level sequence in $MoSe_2$. The A, B excitons result from the transition $d_z \rightarrow d$ at the point $\vec{A}$ of the Brillouin zone. The A′, B′ excitons result from the transition $d_z \rightarrow d$ at point $\vec{H}$. The C exciton results from the transition $d_z \rightarrow d/p$ at the point $\vec{A}$ and D results from the transition $d_z \rightarrow d/p$ at point $\vec{H}$. The α, β peaks result from the $p \rightarrow d/p$ transition at the $\vec{A}$ point. The E feature results from transition at $\vec{L}$ and the F feature from either $\vec{L}$ or $\vec{A}$. The origin of the features *d*, G, H are also assumed to arise from interband transitions. The results of this study do not directly

indicate the exact transitions associated with each feature but eventually help in this respect.

CONCLUSION

A "two-step" halogen vapor transport method has been developed for growing large size crystals of 2H-$MoSe_2$. Conductivity measurements show that intrinsic conductivity begins to dominate at 650°K with a thermal energy gap around 1eV. The measurements of TR and EER spectra of these crystals have enabled us to identify the various features in the spectrum and determine their interband transition energies with a better accuracy. The experimental results agree well with Kasowski's LCMTO band structure model.

ACKNOWLEDGEMENT

The author would like to thank Dr. George J. Goldsmith of Boston College for valuable discussions.

REFERENCES

(1) R. B. Somoano and A. Rambaum, *Phys. Rev. Lett.* 27, 402 (1972).
(2) D. W. Bullett, *J. Phys. C: Solid State Phys.* 11, 4501 (1978).
(3) H. Tributsch, *Solar Energy Material* 1, 257 (1979).
(4) J. A. Wilson and A. D. Yoffe, *Adv. Phys.* 18, 193 (1969).
(5) B. L. Evans, in *Physics and Chemistry of Materials with Layered Structures*, Vol. 4: Electrical and Optical Properties, ed. by P. A. Lee, D. Reidel Publishing, Co. Boston (1976).
(6) A. Anedda and E. Fortin, *Phys. Chem. Solids* 41, 865 (1980).
(7) K. Saiki, M. Yoshimi and S. Tanaka, *Phys. Stat. Sol.* (*b*) 88, 607 (1978).
(8) M. Tanaka, H. Fukutani and G. Kuwabara, *J. Phys Soc. Japan* 45, 1899 (1978).
(9) H. Meinhold and G. Weiser, *Phys. Stat. Sol.* (*b*) 73, 105 (1976).
(10) S. H. El-Mahalawy and B. L. Evans, *Phys. Stat. Sol.* (*b*) 79, 713 (1977).
(11) B. Batz, *Semiconductors and Semimetals* Vol. 9, eds. by R. L. Willardson and A. C. Beer, Academic Press, New York, 316 (1972).
(12) D. E. Aspnes, *Handbook on Semiconductors*, Vol. 2, ed. by M. Balkanski, North Holland, Amsterdam, 109 (1980).
(13) Y. Hamakawa and T. Nishino, *Optical Properties of Solids: New Developments*, ed. by B. O. Seraphin, North Holland, Amsterdam, 255 (1976).
(14) H. Schaffer, *Chemical Transport Reactions*, Academic Press, New York (1964).

(15) R. Fivaz and E. Mooser, *Phys. Rev.* **163**, 743 (1967).
(16) B. L. Evans and R. A. Hazelwood, *Phys. Stat. Sol.* (*a*) 4, 181 (1971).
(17) P. M. Amirtharaj, F. H. Pollak and A. Wold, *Solid State Comm.* **41**, 581 (1982).
(18) A. R. Beal, J. C. Knights and W. Y. Liang, *J. Phys. C: Solid State Phys.* **5**, 3540 (1972).
(19) D. E. Aspnes and J. E. Rowe, *Phys. Rev. Lett.* **27**, 188 (1971).
(20) R. A. Bromley, R. B. Murray and A. D. Yoffe, *J. Phys. C: Solid State Phys.* **5**, 759 (1972).
(21) L. F. Mattheiss, *Phys. Rev. Lett.* **30**, 784 (1973).
(22) J. C. McMenamin and W. E. Spicer, *Phys. Rev.* **B16**, 5474 (1977).
(23) R. V. Kasowski, *Phys. Rev. Lett.* **30**, 1175 (1973).

Learn to *read* with a purpose, and only read the best. That is to say, read that from which you can carry something that enlarges the range of your knowlege, sets your mind working, and quickens your powers of thinking and feeling something far more than mere transient amusement. With a good book before your eyes, knowledge is increased. Thought is set in motion. The worth of a book is measured by what you can carry from it. And that depends also on the spirit in which you read. *Apply your intellect*, read with enthusiasm and pleasure, and you will extract more benefit from what you read.

It is not the quality of reading that counts, but the quality and the intensity of thought that are evoked. The adage that *Time is Money* falls far short of the truth. Time is worth more than money because by its wise employment more wisdom can be secured than money can purchase.

Reading is easy, and *thinking* is hard work. but the one is useless without the other. The reading which counts is reading which, in making a man think, stirs and exercises and polishes the edge of his mind.

LEON GUTTERMAN

STUDY OF PHYSICAL PROPERTIES OF MACROMOLECULES BY A LIGHT SCATTERING METHOD

SHANG-KAI LEE

1. INTRODUCTION

In light scattering experiments, a particle which has a size greater than one twentieth of the wavelength of the incident light can be considered as a macroparticle. The phase of waves scattered from different parts of a macroparticle will not be the same. This is due to the fact that the size of the macroparticle is comparable to the wavelength of the incident light. Hence, the scattered light is affected by the size of particles through interference. We used general purpose polystyrene GPS, high impact polystyrene HIPS and polymethyl methacrylate PMMA as samples of macromolecules and determined their physical properties such as moclecular weight, molecular size, radius of gyration, and virial coefficient by use of light scattering method. The light scattering method is now one of the most valuable tools for the characterization of macromolecules.

In the experiment a He-Ne laser is used as the light source. The optical path is arranged according to the modified compensation method, and the lock-in amplification method is employed in the electronic detecting system.

2. BASIC THEORY

A. Rayleigh scattering and molecular weight of small particals

If we consider an isolated optically isotropic molecule which is small compared with the wavelengh of incident light, and no interaction between the molecules, the scattering of light by molecules can be considered in terms of radiation by dipoles associated with molecules, which are induced by the linearly polarized incident light. The Rayleigh factor is defined as

$$R = \frac{I r^2}{I_0 V} \tag{1}$$

where I and I_0 are intensities of scattered and incident light respectively, V is the scattering volume, and r is the distance from scattering volume to detector.

According to the statistical mechanical theory the isotropic Rayleigh factor by fluctuation in the concentration can be expressed as[1]

$$R_{is} = \frac{\pi^2}{\lambda^4} \beta_T kT \left(c \frac{\partial \varepsilon}{\partial c} \right)_T^2 \tag{2}$$

where β_T is the isothermal compressibility, c and ε are the concentration and dielectric constant of the scattering molecular solution respectively.

When the scattering particles are anisotropic, the scattering is no longer completely vertically plane-polarized, but reinforced by an additional horizontal component. The Cabannes factor is defined as[2,3]

$$f(\Delta) = \frac{R_{total}}{R_{is}},$$

where $R_{total} = R_{is} + R_{anis}$. At a scattering angle of 90° it is given

$$f(\Delta) = \frac{R_{total}(90°)}{R_{is}(90°)} = \frac{3 + 3\Delta_v}{3 - 4\Delta_v}, \tag{3}$$

where $\Delta_v = I_h/I_v$, the depolarization factor for vertically polarized incident light, is the ratio of the scattered intensities with polarization parallel I_h and perpendicular I_v to the plane of observation, respectively. So the Rayleigh factor due to the fluctuations of concentration and anisotropy is

$$R_{conc} = \frac{4\pi^2 n_0^2 (\partial n/\partial c)_T^2 R_g T c}{\lambda^4 N_a (\partial \Pi/\partial c)_T} f(\Delta),$$

where

R_{conc}: Rayleigh factor due to concentration,
n_0 : refraction index of pure solution,
R_g : gas constant,
N_a : the Avogadro's number.

By the Van't Hoff equation the osmotic pressure can be written as

$$\Pi = R_g T c\,(1/M + A_1 c + A_2 c^2 + \ldots), \tag{5}$$

where M is the molecular weight of the dissolved substance, A_1 and A_2 are the first and second virial coefficients.

From eq. (4) we get

$$\frac{Kc}{R_{conc}} = \frac{1}{M} + 2A_1 c + 3A_2 c^2 + \ldots \tag{6}$$

where

$$K = \frac{4\pi^2}{\lambda^4 N_a} n_0^2 \left(\frac{\partial n}{\partial c}\right)_T^2 f(\Delta).$$

B. Light scattering by larger particles

Consider the large molecule to be made up of a large number of submolecules, each of which is small compared with the wavelength and may be considered as a point source of radiation (scatterer).

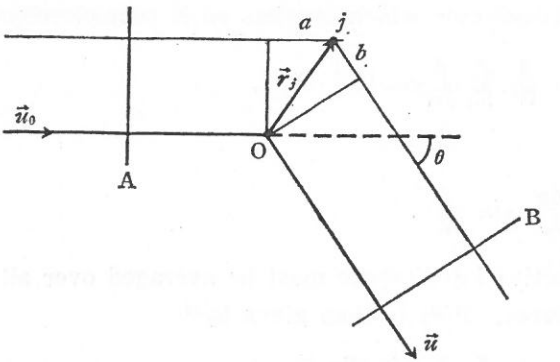

Fig. 1

Let the incident light electric field be propagated in the direction of the unit vector $\vec{u}_0$, and $\vec{u}$ be in the direction of the unit vector of scattered field, 0 be the arbitrary origin, j be the jth scatterer of this system which be observed, then the path difference between the jth molecule and the reference origin is:

$$(a + b) = \vec{r}_j \cdot (\vec{u} - \vec{u}_0).$$

The phase difference ϕ_j is

$$\phi_j = \frac{(a+b)}{\lambda_s} = \vec{r}_j \cdot \vec{n}\left(\frac{2}{\lambda_s} \sin \frac{\theta}{2}\right), \tag{7}$$

where $\vec{n}$ is the unit vector of the direction $\vec{u}_0 - \vec{u}$, λ_s is the wavelength in the solution, i.e., $\lambda_s = \lambda/n_0$.

There may be destructive interference between light waves scattered from different parts of the molecule. The scattering envelop is no longer symmetrical, while the intensity depends on the angle θ.

We define a diminution factor for the interference effect of large size particles

$$P(\theta) = \frac{I(\theta)}{I(0)} \tag{8}$$

where

$I(\theta)$: scattered beam intensity at angle θ,

$I(0)$: scattered beam intensity at $\theta = 0°$.

For a macromolecule which consists on N submolecules[3]

$$P(\theta) = \frac{1}{N^2} \sum_{i=1}^{N} \sum_{j=1}^{N} \cos [S\vec{n} \cdot \vec{r}_{ij}],$$

where

$$S = \frac{4\pi}{\lambda_s} \sin \frac{\theta}{2}.$$

The destructive interference must be averaged over all orientations of N scatterers. $P(\theta)$ is then given by[4]

$$P(\theta) = \frac{1}{N^2} \sum_{i=1}^{N} \sum_{j=1}^{N} \frac{\sin (Sr_{ij})}{Sr_{ij}}. \tag{9}$$

We may expand eq. (8) into a power series to yield

$$\begin{aligned} P(\theta) &= \frac{1}{N^2}\left[N^2 - \frac{1}{3!} \sum_{i=1}^{N} \sum_{j=1}^{N} (S^2 r_{ij}^2)\right. \\ &\quad \left. + \frac{1}{5!} \sum_{i=1}^{N} \sum_{j=1}^{N} (S^4 r_{ij}^4) + \ldots\right] \\ &= 1 - \frac{S^2}{6N^2} \sum_{i=1}^{N} \sum_{j=1}^{N} r_{ij}^2 + \ldots. \end{aligned} \tag{10}$$

Now consider an important parameter, the radius of gyration, which yields information about a molecular size parameter. The radius of gyration is essentially the root-mean-square radius of a macromolecule. Let R be a vector locating the center of mass of a molecule and $\vec{r}_i$ be a vector locating submolecule i with mass m_i. Then by definition

$$R_G^2 = \frac{\sum_{i=1}^{N} m_i(\vec{r}_i - R)^2}{\sum_{i=1}^{N} m_i}. \tag{11}$$

R_G may be calculated as long as the shape of the molecule is as a randomly Gaussian coil particle

$$R_G^2 = \frac{\overline{d^2}}{6} \tag{12}$$

where $\overline{d^2}$ is the mean square length between the ends of the polymer chain.

C. Measuring molecular weight, radius of gyration, and first coefficient by the Zimm plot method[5]

Consider eq. (6). For dilute solutions the higher order terms can be neglected. Then

$$\frac{R_{\theta conc}}{Kc} = \frac{1}{M} + 2A_1 c. \tag{13}$$

For a large particle and from eq. (8)

$$\frac{Kc}{R_\theta} = \frac{1}{MP(\theta)} + \frac{2A_1 c}{P(\theta)}. \tag{14}$$

In the limit of zero concentration

$$\left(\frac{Kc}{R_\theta}\right)_{c\to 0} = \frac{1}{MP(\theta)}. \tag{15}$$

The reciprocal $P(\theta)$ can be approximated from eq. (10)

$$\frac{1}{P(\theta)} = 1 + \frac{S^2}{3} R_G^2 + \ldots. \tag{16}$$

Then, eq. (15) can be written by

$$\left(\frac{Kc}{R_\theta}\right)_{c\to 0} = \frac{1}{M}\left(1 + \frac{16\pi^2}{3\lambda_s^2} R_G^2 \sin^2\left(\frac{\theta}{2}\right) + \ldots\right). \tag{17}$$

And in the limit of zero angle $P(\theta) \to 1$ eq. (14) can be written by

$$\left(\frac{Kc}{R_\theta}\right)_{\theta\to 0} = \frac{1}{M} + 2A_1 c. \tag{18}$$

Finally in the limit of both zero angle and zero concentration

$$\left(\frac{Kc}{R_\theta}\right)_{\substack{c\to 0 \\ \theta\to 0}} = \frac{1}{M}. \tag{19}$$

The method most commonly used to extract M from scattering data utilizes a construction known as the Zimm plot. The quantity Kc/R_θ is ploted versus $BC + \sin^2(\theta/2)$, B being an arbitary constant equal to or less than $1/c$ which was chosen to provide a convenient spread of the data on the grid-like graph which is obtained. A typical Zimm plot, shown as Fig. 2, is made by joining all points of equal concentrations and extrapolating to zero angle, and then all points measured at equal angles and extrapolating these to zero

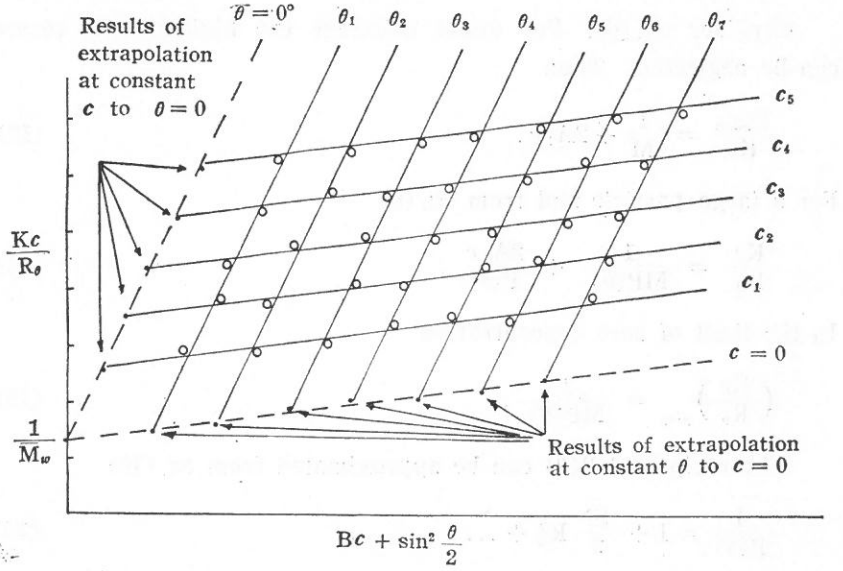

Fig. 2

concentration.

This is done for each concentration and each angle and the extrapolated points are the lines of $\theta=0$, (eq. (18)) and $c=0$, (eq. (17)). Both lines, on extrapolation to the axis, should intersect at the same point. The intercept is then $(M)^{-1}$, the slope of the line of $\theta=0$ yields A_1, then

$$A_1 = \frac{1}{2} K\left[\left(\frac{c}{R_\theta}\right)_{c_2} - \left(\frac{c}{R_\theta}_{c_1}\right)\right]_{\theta\to 0} \Big/ c_2 - c_1 . \tag{20}$$

and R_G^2 is obtained from the slope of the line of $c=0$, i.e.,

$$R_G^2 = \frac{3\lambda^2}{16\pi^2 n_0^2} \times \left(\frac{\text{slope}}{\text{intercept}}\right)_{c\to 0} . \tag{21}$$

In this general sense, one can not assign a unique molecular weight to macromolecules, because even the individual molecules of a certain polymer are of different sizes. The average molecular weight is defined by[6]

$$\overline{M} = \frac{\sum_i n_i M_i^a}{\sum_i n_i M_i^{a-1}} . \tag{22}$$

when

$a = 1$ be numbers average molecular weight $\overline{M}_n$,

$a = 2$ be weight average molecular weight $\overline{M}_w$,

$a = 3$ be z average molecular weight $\overline{M}_z$.

From different $\overline{M}$ values the molecular weight distribution can be determined.

If only one volume element is considered, eq. (19) becomes

$$\lim_{\substack{\theta\to 0 \\ c\to 0}} R_{\theta i} = K c_i M_i .$$

and

$$\frac{\sum_i R_{\theta i}}{\sum_i K c_i} = \frac{\sum_i c_i M_i}{\sum_i c_i} .$$

But $\sum_i R_{\theta i} = R_\theta$, $\sum_i c_i = c$.

$$\frac{R_\theta}{Kc} = \frac{\sum_i n_i M_i^2}{\sum_i n_i M_i}.$$

So that the molecular weight obtained from light scattering is the weight average $\overline{M}_w$.

3. APPARATUS AND EXPERIMENTAL METHOD

A. The optical system

In Fig. 3, the light beam comes from the laser L which emits light of 6328Å wavelength and linear horizontal polarization. The light is modulated with a fixed frequency of 989 Hz by passing through the chopper CH and is inverted from horizontal to nearly

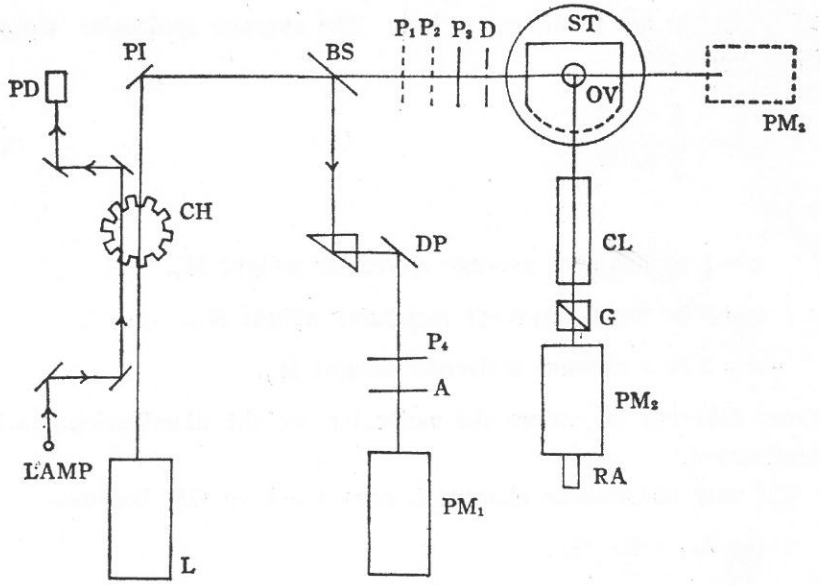

Fig. 3. The optical system of the apparatus.

BS : Beam splitter	P_1, P_2, P_3, P_4, A: Polarizer
CH : Chopper	PD: Photodiode
CL : Collimator	PI: Polarization inverter
D : Diaphragm	PM_1, PM_2: Photomultiplier XP-1117
DP : Diffuse paper	RA: Rotating arm
L : Laser (He-Ne 4 mw)	OV: Oil vessel

vertical polarization by the polarization inverter PI. Then the light passes through the beam splitter BS and the polarizer P_3, which keep the light at vertical polarization, and through the diaphragm D into the solution cell which is in an oil vessel. The polarizers P_1 and P_2 are used only to determine the intensity of incident light I_0.

The intensity of the light reflected from BS, the so called monitor ray, is decreased by diffuse paper DP and can be adjusted by the polarizer P_4 and the analyzer A. PM_1 and PM_2 are used to measure the intensity of the monitor ray and the scattered light, respectively. PM_2 is mounted on a rotary steel arm RA, attached horizontally to the center of the steel table. Therefore the scattered light can be observed at various angles; such an observation is indispensable in studying the macromolecule properties by light scattering. In the direction of observation, a collimator confines the volume of scattering. A Glan-Thompson prism G is placed between the collimator and PM_2 when the depolarization factor is measured.

B. The electronic system

The scattering signal detected by PM_2 is fed into a lock-in amplifier (Brookdeal Co.). The monitor signal detected by PM_1 is fed into another lock-in amplifier (home made). The signals from both amplifiers are subjected to conventional d.c. integration. The purpose of this is to improve the S/N ratio. Finally, the integrated voltages are fed into the digital multimeter DMM. Each reading from the DMM gives the ratio of the scattering intensity to the intensity of the monitor ray. Therefore none of the measurements is influenced by the fluctuation of the laser light. The ratio is read immediately after the integration is finished.

All the experimental data are repeated five times with the phase switch setting to position 0° and then π, respectively. Both measured results of the DMM ratio in different positions are averaged and thereby the not precisely known zero point of the lock-in amplifier is eliminated. The block diagram of the electronic system is shown on Fig. 4.

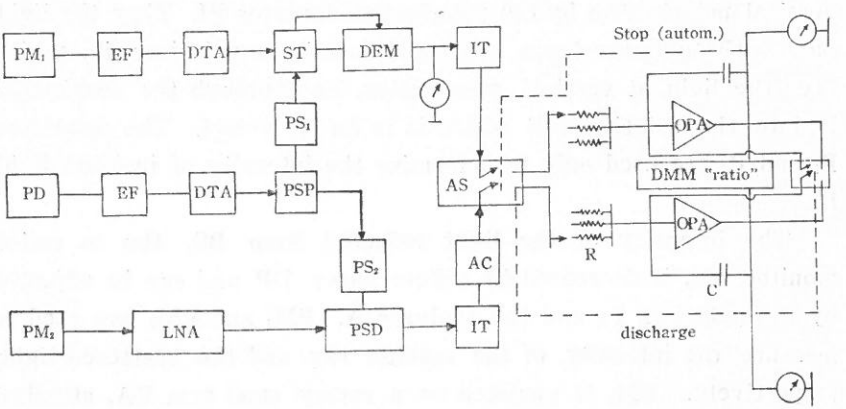

Fig. 4. Block diagram of the electronic system.

EF	: emitter follower	DTA	: double tuned amplifier
IT	: impedance transformer	OPA	: operational amplifier
DEM	: demodulator	ST	: Schmitt trigger
LNA	: low noise amplifier (Brookdeal Model 450)	PSD	: phase sensitive detector (Brookdeal Model 411)
PS_2	: phase shifter (Brookdeal Model 421)	AC	: automatic control circuit
PS_1	: phase shifter	AS	: automatic switch
PSP	: phase splitter	DMM	: digital multimeter (Systron-Donner Model 7110)

C. Experimental method

The experimental determination of the Rayleigh factor R_{conc} is obtained by subtracting R of the pure solvent from R of the solution with a given concentration, i.e.,[5]

$$R_{conc} = R_{solution} - R_{solvent}.$$

A small particle solute of N-octane (M=114) dissolved in benzene is taken. Observations of scattering at different angles due to the pure solvent $R_{sv}(\theta)$ and to the solution $R_{so}(\theta)$ are made. $R_{so}(\theta) - R_{sv}(\theta)$ should show the characteristics of small particle scattering. Theoretically $R_{so}(\theta) - R_{sv}(\theta)$ should be independent of the observation angle θ. These experimental data are listed in the next section.

The Rayleigh factor $R_{90} = F_s l/(F_0 \Omega l)$ is obtained by measuring separately the scattering flux F_s, the incident flux F_0, the solid

angle Ω and the effective length l of the laser beam for scattering. The main problem of the R_{90} determination is the enormous difference between the magnitude of F_0 and F_s, the orders of magnitude are 1 and 10^{-10}, respectively.

The index of refraction of the solvent n_{sv} and that of the solution n_{so} can be measured by the Abbe refractometer with the laser beam as a light source. Then the magnitude of dn/dc can be approximately given as $\Delta n/\Delta c$ where $\Delta n = n_{so} - n_{sv}$ and Δc is the increment in concentration of the solution.

In this experiment the intensity of the scattered light due to the macromolecules is measured. The experimental procedures are as follows: First, record the intensity reading of pure benzene on the DMM at 90°. Then record the respective intensity reading of pure solvent and a certain concentration solution on the DMM at different angles. The subtraction of the reading of pure solvent and concentration solution at any angle is the scattered intensity exhibited by macromolecules at that angle. By comparing to the R_{90} of benzene, we can calculate the value of R_θ at that angle.

Three macromolecules which are provided by PAULI (保利) Co. are studied in this experiment. They are the general purpose polystyrene (GPS), the high impact polystyrene (HIPS) and the polymethyl methacrylate (PMMA). All of them are randomly coiled high polymers.

The solvents for GPS and HIPS are toluene, but for PMMA, the solvent is methyl-ethyl-ketone (MEK). The polymer solution must be purified by filtration or by centrifugation. In our experiments, the efficiency of purification of solution by centrifugation is better than by filtration. So, all solutions used in experiments were centrifuged at 11,000 rpm for forty minutes.

4. EXPERIMENTAL RESULTS

A. Calibrations of instrumental angular distribution of scattering

Small moles of N-octane ($CH_3(CH_2)_6CH_3$) were used as a calibrator. The scattering of these molecules at every angle should be

the same if the instruments were properly aligned.

The scattered intensities of N-octane observed at several angles are listed as follows.

Table 1. Scattered Intensity of N-octane

Angle	$[R_{so} - R_{sv}] \times 10^4$
42.5°	243±31
58°	238±14
74°	242±10
90°	235±17
107°	220±13
123°	222±16
138°	216±18

R_{so}: reading on DMM when solution is in cell.
R_{sv}: reading on DMM when solvent is in cell.

B. Zimm plot for GPS

A Zimm plot for GPS at 21.5°C with centrifuging at 11,000 rpm. for forty minutes is shown in Fig. 5. From this figure, the weight average molecular weight, size and first virial coefficients of GPS are obtained and listed in Table 2.

Table 2. Result for GPS

Weight-average molecular weight	$\overline{M}_w = (2.84 \pm 0.26) \times 10^5$ g mole^{-1}
Radius of gyration	$R_G = (623 \pm 33)$ Å
Root-mean square length between ends of chain	$\sqrt{\overline{d^2}} = (1{,}527 \pm 76)$ Å
First virial coefficient	$A_1 = (8.43 \pm 0.42) \times 10^{-4}$ mole g^{-2} cm^3

C. Zimm plot for HIPS

A Zimm plot for HIPS at 20.5°C with centrifuging at 11,000 rpm. for forty minutes is shown in Fig. 6. From this figure, the weight average molecular weight, size and first virial coefficients of HIPS are obtained and listed in Table 3.

Table 3. Result for HIPS

Weight-average molecular weight	$\bar{M}_w = (2.46 \pm 0.16) \times 10^5$ g mole^{-1}
Radius of gyration	$R_G = (1{,}246 \pm 62)$ Å
Root-mean square length between ends of chain	$\sqrt{\overline{d^2}} = (3{,}053 \pm 153)$ Å
First virial coefficient	$A_1 = (1.04 \pm 0.06) \times 10^{-3}$ mole g^{-2} cm^3

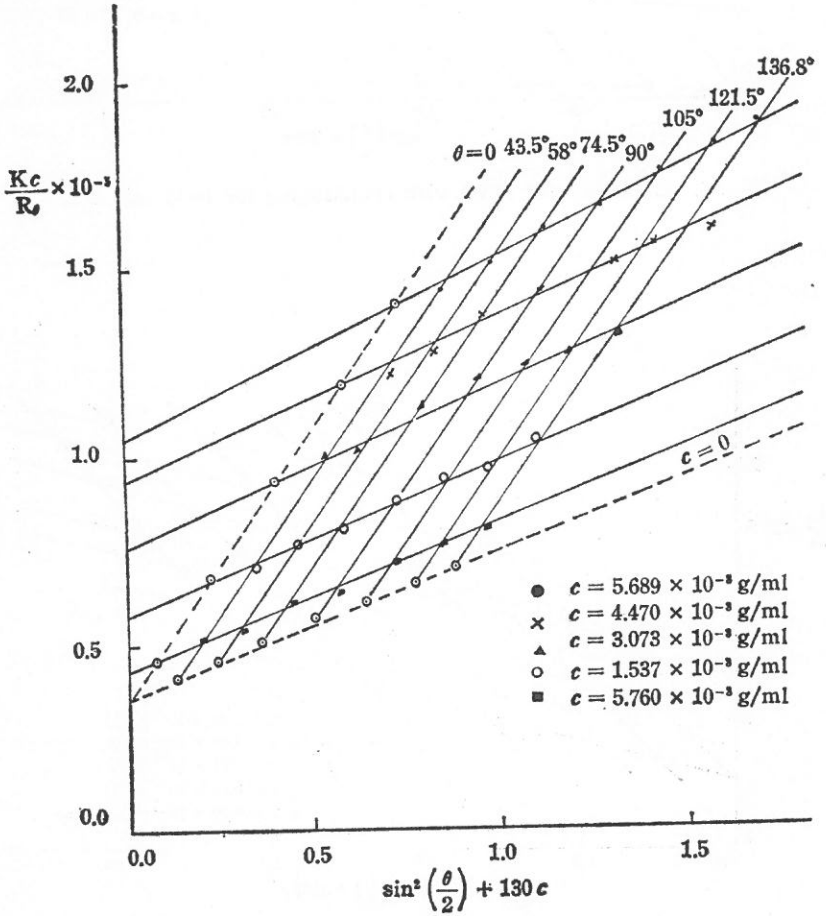

Fig. 5. Zimm-plot for GPS with centrifuging for forty minutes.

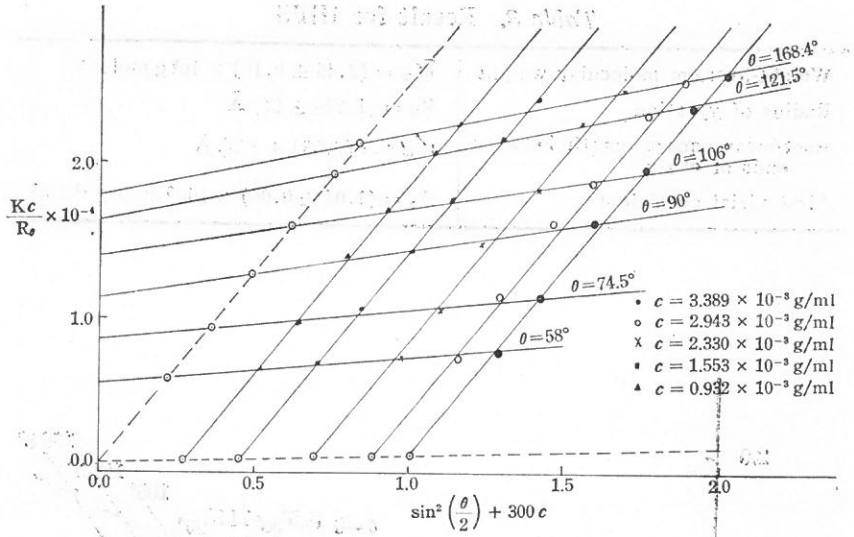

Fig. 6. Zimm-plot for HIPS with centrifuging for forty minutes.

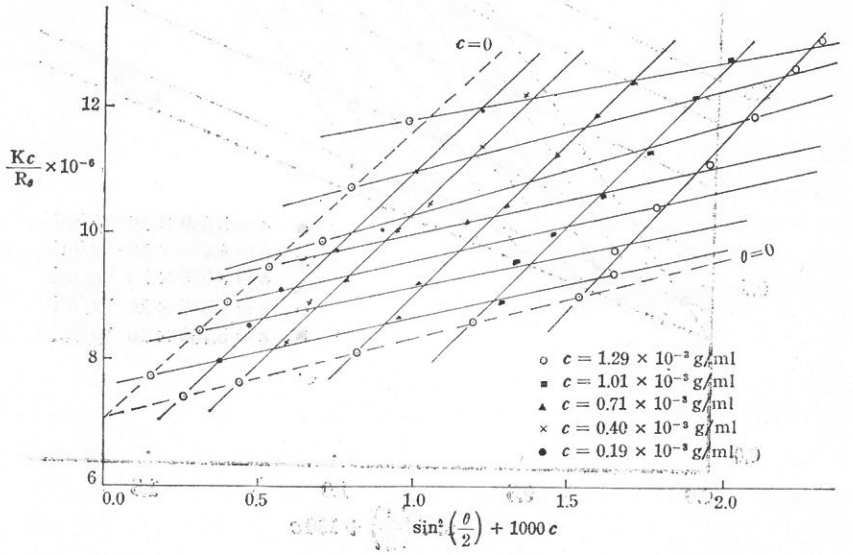

Fig. 7. Zimm-plot for PMMA with centrifuging for forty minutes.

D. Zimm plot for PMMA

A Zimm plot for PMMA at 20.5°C with centrifuging at 11,000 rpm. for forty minutes is shown in Fig. 7. From this figure, the weight average molecular weight, size and first virial coefficients of PMMA are obtained and listed in Table 4.

Table 4. Result for PMMA

Weight-average molecular weight	$\bar{M}_w = (1.41 \pm 0.13) \times 10^{-5}$ g mole^{-1}
Radius of gyration	$R_G = (539 \pm 37)$ Å
Root-mean square length between ends of chain	$\sqrt{\bar{d}^2} = (1{,}320 \pm 40)$ Å
First virial coefficient	$A_1 = (4.68 \pm 0.47) \times 10^{-7}$ mole g^{-2} cm^3

5. DISCUSSIONS

From Table 1 the scattered intensities of N-octane at different angles are slightly different from one another. The standard deviation of scattered light is greater at 42.5° than at any larger angle. This is due to the bigger contribution of scattering intensity from dust particles at low angles. In the region of the standard deviation of each quantity, the scattered intensities at various angles can be seen to be the same. This shows that we have proper alignment of the apparatus.

The depolarization ratio $\Delta_v = I_h/I_v$ for all three samples are measured at every observation angle. The values of I_h which are almost equal to background of our apparatus are too small to be detected by our apparatus. The measured values of I_v are much greater than I_h ($I_v > 1{,}000\, I_h$). Then, $\Delta_v \sim 0$ which implies that the Cabannes factor is approximately equal to 1 for each angle. Therefore, the scattered intensities do not have to be corrected at observation angles for anisotropy which is usually expressed by the Cabannes factor.

Values for (dn/dc) of GPS at a wavelength 6238Å are too small to be accurately measured by an Abbe refractometer. The possible

error due to this value is 5%. The error due to the (dn/dc) measurement will influence greatly the molecular weight determination, because of (dn/dc) as a squared term in eq. 6. Since the (dn/dc) measurement is so important, we suggest that a differential refractometer, which permits the determination of (dn/dc) to a high accuracy up to 10^{-5}, should be used in future experiments.

The Zimm-plot can be considered as a criterion of the validity of the experiment. In Figs. 5, 6 and 7 the experimental points on the Zimm-plots are in good agreement with the prediction of the theory presented in section 2.

The approximate value of $\bar{M}_w$ of GPS supplied by Pau Li Co. is 2.9×10^5 g mole^{-1} and our experimental result is $(2.84\pm0.14)\times10^5$ g mole^{-1}. This shows that our experimental results coincide with the theory.

From our experiments, we determined that the value of $\bar{M}_w$ of HIPS is $(2.46\pm0.16)\times10^5$ g mole^{-1} and that of PMMA is $(1.41\pm0.13)\times10^5$ g mole^{-1}.

We also did the same experiment using a spherical protein xp-12 as a sample. We found that the result produced a very good Zimm-plot. But we did not know the concentration of xp-12.

The duration of centrifuging affects position of points on the Zimm-plot; that is, the influence of dust (or extraneous material) is a major problem. As the duration of the centrifuging is forty minutes, experimental results on the Zimm-plot are better than those from any other duration. However, even after centrifuging at 11,000 R.P.M. for forty minutes, experimental points on the Zimm-plot are still somewhat scattered. This is caused by carelessness in the experiment, such as using a cell which is not clean enough or using a not precisely controlled concentration of solutions.

In Figs. 5, 6 and 7, a few experimental points do not coincide with the straight line obtained by a least square method. There might be two reasons for this digression. One is that the transmission coefficients of different thin glass pieces are not the same.

(Their average difference is 0.45%.) The other is that when rotating the arm of the steel table to different observation angles, the position of the arm at different times at a certain observation angle can be different. This error is less than 2%.

Here we use the method of light scattering to measure $\overline{M}_w$ of a polymer, we suggest that we can also use an osmotic pressure method to determine $\overline{M}_n$ of a polymer, and use the ultracentrifuge method to determine $\overline{M}_z$. Then from $\overline{M}_n$, $\overline{M}_w$, and $\overline{M}_z$ of the polymer, we can find the distribution function of the molecular weight of the polymer. Therefore, from this distribution function we can find more of its physical properties.

A special advantage of the light-scattering method we used in this paper lies in the fact that from a series of measurements we obtain the weight-average molecular weight, the radius of gyration, the first virial coefficient, and the particle size. Data obtained in this paper is valuable to polymer science. For example, $\sqrt{\overline{d^2}}$ (root mean square length between ends of the polymer chain), can presently not be obtained by any other direct measurement.

Furthermore, the scattered intensity is proportional to molecular weight, and influences of stray light and dust particles, are smaller compared with the strong scattered light. Therefore, the accuracy of our light-scattering experiment increases with increasing molecular weight. This is in contrast with the other methods of determination of molecular weight, in which the accuracy diminishes with increasing molecular weight.

Owing to these advantages, the light-scattering method has become important and is now one of the most valuable means for the characterization of macromolecules.

REFERENCES

(1) F. J. Lin, *Fu Jen Studies* **15**, No. 11. (1977).
(2) P. Doty, *J. Polymer Science*, **3**, No. 5 750-771 (1948).
(3) P. Debye, and E. S. Elyash, *Technical Report GR-7* (1944).
(4) D. A. McQuarrie, *Statistical Mechanics* (1976).
(5) B. H. Zimm, *J. Chem. Phys.*, **16**, 1093 and 1099 (1948).
(6) M. L. Miller, *The Structure of Polymers*, Reinhold Publishing Corporation, New York (1966).

I believe in the force of example. The wise men of *ancient China*, when they wished to disseminate the highest virtues among mankind, first ordered well their own states. Wishing to order their states well, they first regulated their own families. Wishing to regulate their families, they first sought to cleanse their own hearts. They first sought to be sincere in their thinking. Wishing to be sincere in their thinking they first extended their knowledge to the utmost.

Reform begins at home and Utopia is nowhere except in the clean heart and understanding mind.

WILL DURANT

QUASICLASSICAL TRAJECTORY STUDY OF THE F+H_2 REACTION: FOURIER ANALYSIS OF PRODUCT DISTRIBUTIONS

FRANK E. BUDENHOLZER SVD and LIN-SHENG HUANG

I. INTRODUCTION

Quasiclassical trajectory calculations have provided an important tool in the study of simple chemical reactions. Product angular distributions can be compared with the results of beam experiments, product energy distributions with the results of product velocity analyses or with the results of chemiluminescence experiments. However the best procedure to display the information contained in the product distributions obtained from trajectory studies is still an open question.

In 1977 Trular and Blais[1] and Gislason and Sachs[2] independently suggested expanding the cross section as a Legendre series. More recently Gislason and coworkers have suggested using Fourier series to expand the differential cross section[3] and the product energy distributions.[4] Until now these Fourier analyses have been limited to model calculations[3] and the analysis of the product distributions of the $H + H_2$ reaction.[4,5] We are at present in our laboratory developing programs to carry out various types of trajectory studies. As part of this project we have applied the Fourier expansion technique to the well studied $F + H_2$ reaction. We feel that this study demonstrates the advantages of the Fourier expansion technique even when the number of trajectories is fairly small.

II. TRAJECTORY CALCULATIONS

6000 trajectories were run over the "Muckerman V" potential energy surface.[6] The initial translational energy was 3.0 kcal/mole, initial rotational energy 0.12 kcal/mole, and the initial vibrational

energy the zero point energy of H_2. All other parameters were selected randomly. Trajectories were calculated using the QCPE program "A+BC".[7] Of the 6000 trajectories runs, 2029 were reactive giving a total cross section of 4.25Å^2. (This cross section is somewhat large. This was found to be due to a poor selection of certain program parameters. However tests showed that the product distributions were not noticibly affected.)

The product angular distribution was expanded in a Fourier series and smoothed using the so-called Gaussian filter.

$$\langle I(\vartheta) \sin \vartheta \rangle = \sum_{n=1}^{\infty} a_n \sin n\vartheta \, e^{-n^2 \Delta\vartheta^2 / 4} \tag{1}$$

Here $I(\vartheta)$ is the differential cross section, ϑ the polar scattering angle, $\{a_n\}$ the Fourier coefficients and $\Delta\vartheta$ a smoothing parameter. Prescriptions to calculate a_n and $\Delta\vartheta$ are contained in reference 3.

Product energy distributions, $P(Z_i)$, were expanded in a reduced variable Z_i,

$$Z_i = \frac{E_{tot}}{E_i} \tag{2}$$

where the index i indicates translation (t), vibration (v) or rotation (r) and E_{tot} is the total energy available to products.

$$\begin{aligned} P(Z_v) &= 1 + \sum_{n=1}^{M} a_n \cos(n\pi Z_r) \\ P(Z_t) &= \sum_{n=1}^{M} b_n \sin(n\pi Z_t) \\ P(Z_r) &= 1 + \sum_{n=1}^{M} a_n \cos(n\pi Z_r) \end{aligned} \tag{3}$$

Prescriptions for calculation and more detailed explanations are found in references 3 and 5. The expansions of eq. (3) may be smoothed, however it was found to be unnecessary in this study. The results are shown in Figs. 1 and 2. The error bars indicate the 68% confidence levels.

III. DISCUSSION

A number of advantages of the Fourier expansion method have

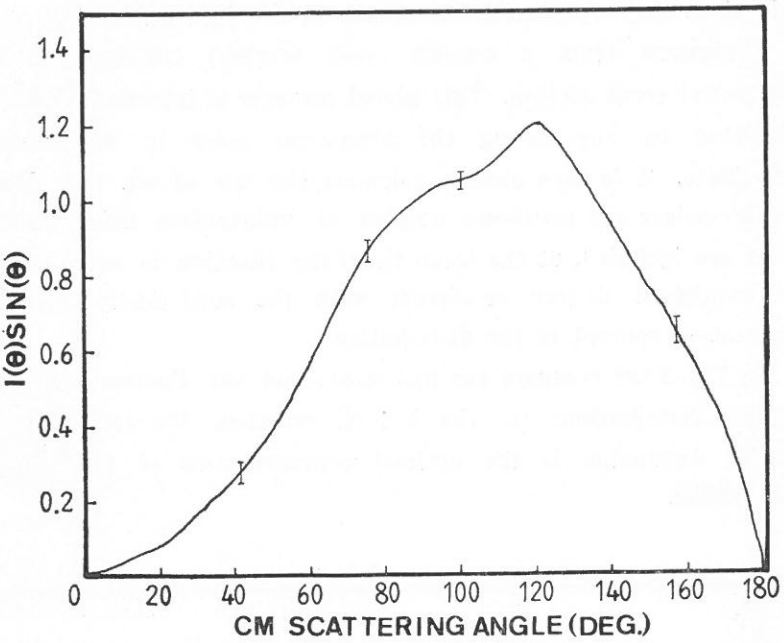

Fig. 1. Reactive differential cross section $I(\vartheta)\sin\vartheta$ for the $F+H_2$ reaction, expanded in a Fourier series as given by eq. (1). Initial conditions and procedures for calculating trajectories are given in the text. Uncertainties are 68% confidence limits.

already been pointed out. Among them is the fact that continuous distributions are obtained as is expected from a classical calculation and that uncertainties can clearly be assigned.

We argue that a further advantage of the method is that it provides the optimal expression of the information available from a limited number of trajectories. The problem in interpreting bar graphs is that it is difficult to decide what information is significant and what is due to statistical fluctuations inherent in any Monte Carlo calculation. Thus there is a need for an unambiguous procedure to "draw the best line" through the histogram distribution. Eq. (1) provides such a procedure.

Gislason[3] defines a smoothness function Z,

$$Z = \frac{\pi}{2}\int_0^{\pi}\left[\frac{\alpha(I(\vartheta)\sin\vartheta)}{\alpha\vartheta}\right]^2 d\vartheta \qquad (4)$$

which is a single parameter measure of the information (as seen as deviations from a smooth cross section) contained in the differential cross section. This global measure of information can be calculated by considering the statistical noise in the Fourier coefficients. Z is then used to calculate the $\Delta\vartheta$ of eq. (1). Using this procedure the maximum number of information laden Fourier terms are included, at the same time the function is smoothed to the maximum degree consistent with the statistically expected information content of the distribution.

In Fig. 3 we compare the histogram and the Fourier expanded angular distributions for the F + H_2 reaction. We feel that the Fourier expansion is the optimal representation of the angular distribution.

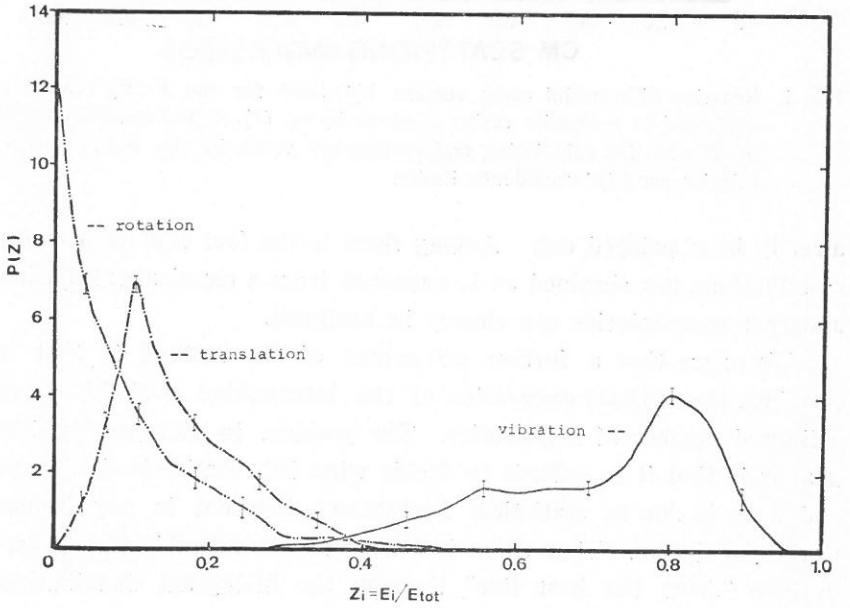

Fig. 2. Product energy distributions from the classical trajectory study of F+H_2 expanded according to eq. (3). Initial conditions are described in the text. Uncertainties are 68% confidence limits. Solid line, product vibration; dot-dash, translation; dot-dot-dash, product rotation. Note the significant degree of vibrational excitation.

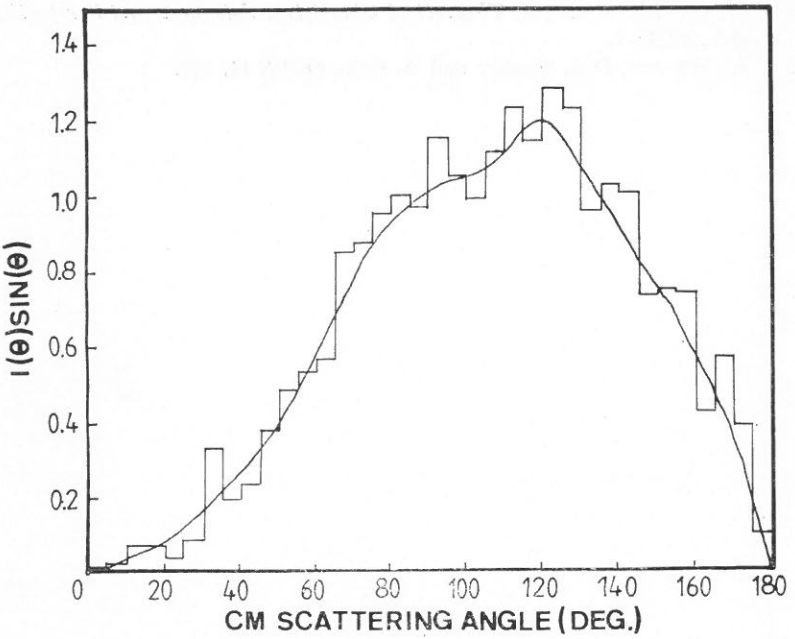

Fig. 3. The reactive differential cross section $I(\vartheta)\sin\vartheta$ Fourier expanded according to eq. (1). Also shown is the angular distribution "binned" at five degree intervals.

Acknowledgement

This research has been supported by a grant form the National Science Council of the Republic of China. Thanks to Mr. Min-Shung Chang for assistance in programming.

REFERENCES

(1) D. G. Truhlar and N. C. Blais, *J. Chem. Phys.* **67** (1977) 1532.
(2) E. A. Gislason and J. G. Sachs, *Chem. Phys. Lett.* **52** (1977) 270.
(3) A. Kosmos, E. A. Gislason and A. D. Jorgensen, *J. Chem. Phys.* **75** (1981) 2884.
(4) E. A. Hildebrand, A. D. Jorgensen and E. A. Gislason, preprint supplied by the authors.
(5) E. A. Hildebrand, A. D. Jorgensen and E. A. Gislason, in *Potential Energy Surfaces and Dynamics: Calculations for Chemical Reactions and Energy Transfer Collisions*, edited by D. Truhlar (Plenum, New York, 1981), pp. 421-430.

(6) James T. Muckerman, *Theoretical Chemistry: Advances and Perspectives*, **61A** (1981) 5.
(7) S. Chapman, D. L. Bunker and A. Gelb, *QCPE* **11**, 273.

COAL FLY ASH AS A PLASTIC FILLER

SHANG-SHING P. CHOU and CHUNG-BIN CHU

ABSTRACT

Coal fly ash generated from thermo-power plants was used as a plastic filler for polypropylene and urea-formaldehyde resin. Polypropylene filled with fly ash of different mesh sizes was compression molded to give products showing greater tensile strength than those filled with the conventional calcium carbonate filler. The chemical resistance and water absorptivity of fly ash filled polypropylene were also found to be excellent. Pigments could be added to give products of different colors. On the other hand, urea-formaldehyde resin filled with fly ash was less satisfactory than the one filled with α-cellulose. This study points out a possible way of economically disposing of large quantities of fly ash.

INTRODUCTION

Since the oil crisis began in the early 1970's many countries in the world started looking eagerly for alternative energy sources. In order to cut down oil imports the Republic of China has decided to use more coal and nuclear energy for its power supply in the future. The world's coal reserves are much more abundant than oil, but there is one technical problem to be solved in the generation of electricity by coal—the disposal of the waste product fly ash.

Fly ash is produced as an unburned waste in the amount of 5 to 20 percent of the coal fed to the boiler. These small particles will cause severe air pollution if they are discharged into the air. The power plants must absorb the costs of labor and equipment for the disposal of these ashes to ecologically acceptable sites. The use of fly ash for more constructive purpose would be desirable. Fly ash is a complex mixture of materials; the major components being silica, alumina, iron oxide and unburned carbon. Fly ash has been used as a concrete additive[1] and for highway paving[2]. There have also been some recent reports on the use of fly ash as a filler for certain plastics such as polypropylene[3], polyvinyl

chloride[4], nylon 66[5], and polystyrene[6]. The added filler not only lowered the costs of these plastics but in some cases also improved the physical properties of the products.

It is estimated that if 30 percent by weight of fly ash could be added to the common plastic materials used in Taiwan, five million tons of fly ash would be consumed in 1983 alone. This could solve the problem of disposing fly ash and also save a fair amount of money which would have to be spent using conventional plastic fillers. We report here our studies on using fly ash as the filler for polypropylene and urea-formaldehyde resin, the former being a thermoplastic and the latter a thermosetting polymer. It is hoped that the results obtained from these studies can be applied to other plastic materials.

MATERIALS AND METHODS

The polypropylene used was PC 366 made by Taiwan Polypropylene Co.. Its T_m is about 170°C and it has an average molecular weight of 200,000 as determined by viscosity measurement. The fly ash was provided by the Taiwan Power Co.. It was obtained from burning Australian coal and has the following chemical composition: SiO_2 (44%), Al_2O_3 (21%), Fe_2O_3 (7%), TiO_2 (4%), MgO (1%), unburned carbon (17%) and other oxides in smaller quantities.

Fly ash filled polypropylene was prepared by mixing polypropylene, fly ash, dioctylphthalate (DOP, a plasticizer), butylated hydroxytoluene (BHT, an antioxidant), stearic acid (a lubricant), stearates of barium, lead and calcium ions (heat and light stabilizers), and other additives in a blender. After blending the mixture was heated in a beaker at 190–200° until melted. The melt was kept at this temperature for 30 minutes with constant mechanical stirring and was compression molded at 130–140°C with a pressure of 210 Kg/cm^2 for 10 minutes. Products were prepared with various ratios of components and with fly ash of varying particle sizes. The resulting products were examined for tensile strength (as determined by ASTM method D638), water absorptivity (ASTM method D570) and resistance to chemicals (ASTM method D543).

The urea-formaldehyde resin was prepared as follows. Urea (11.4 g) was added slowly and with mechanical stirring to 28.4 g of a 37% aqueous formaldehyde solution (low methanol content) at 20–25°C. The pH of the mixture was adjusted to 7.4–7.5 by adding triethanolamine (~0.02 g). After refluxing for 3–4 hours the milky solution was cooled to room temperature. Most of its water was removed by rotary evaporation at 35–40°C/22–30 mmHg. The resulting solution (pH 7–7.8) weighed 9.1 g and had a viscosity of 150–250 c. p.. This resin was mixed thoroughly with 20% by weight of fly ash and was dried in an oven at 60°C for 2 days. The dried material was ground, blended, sieved into different sizes, and stored in a desiccator before use. The molding powder prepared above was placed in a mold and was heated at 75°C for 10 seconds with 100 kg/cm² of pressure. This procedure was repeated three times in order to remove all the air bubbles from the resin. The compression molding was continued for 30 minutes at 140-145°C and 150 kg/cm² of pressure. This resin was slowly cooled to room temperature in 6 hours while keeping the pressure at 150 kg/cm². The impact strength and the tensile strength of this fly ash filled urea-formaldehyde resin were determined by the ASTM D256 (Izod notched) and D638 methods, respectively. Its resistance to chemicals and water absorptivity were measured in a manner similar to those for fly ash filled polypropylene.

RESULTS AND DISCUSSION

A. Polypropylene Filled with Fly Ash

Since there were many ingredients involved in the preparation of fly ash filled polypropylene, it was not possible to study the effect of individual components on the properties of the product. Thus, the relative ratios of all additives were kept roughly the same while the ratios of polypropylene and fly ash were varied. Some representative formulations of fly ash filled polypropylene are shown in Table 1.

Fly ash is a mixture of compounds of different particle sizes.

Table 1. The Weight Ratios of Ingredients in Fly Ash Filled Polypropylene

Ingredients \ Fly ash content	10%	20%	30%
Polypropylene	100	100	100
Fly ash	13	30	54
Zinc oxide	2	2	2
DOP	5	7	9
BHT	2	2	2
Stearic acid	6	7	9
Stearates	2	2	2

Table 2. The Effect of Particle Size on the Tensile Strength of Fly Ash Filled Polypropylene

Particle size \ Fly ash content	Tensile strength (kg/cm^2)		
	10%	20%	30%
100 mesh	124.5	134.9	114.7
250 mesh	123.3	116.5	134.9
400 mesh	190.5	179.7	145.3

It is likely that the particle size of fly ash will have significant effects on their molecular interactions with polypropylene. Thus, the fly ash was sieved to give three fractions of different mesh sizes, 100 mesh, 250 mesh and 400 mesh, where the larger numbers indicate increasingly small particle sizes. The tensile strengths obtained with these materials are shown in Table 2. It is clearly seen that (1) no matter what the percentage of fly ash is in each product, the smaller the particle size, the larger the tensile strength is; (2) for fly ash of 400 mesh size the tensile strength is greatest when its percentage weight is 10%, but for fly ash of other particle sizes the optimal percentage weights are different; (3) the best result is obtained when polypropylene is filled with 10% by weight of fly ash of 400 mesh size.

The most common filler for polypropylene is calcium carbonate

whose efficacy as the filler was compared directly with fly ash. Polypropylene filled with calcium carbonate was prepared in exactly the same manner as the fly ash filled polypropylene. The tensile strength obtained with calcium carbonate filler of 400 mesh is shown in Table 3. It is clearly seen that (1) calcium carbonate has a deleterious effect on the tensile strength of polypropylene; the greater the content of calcium carbonate, the worse the product is; (2) fly ash is a much better filler than calcium carbonate for polypropylene in all weight percentages studied; (3) polypropylene filled with 20% of fly ash (400 mesh size) has about the same tensile strength as the pure polymer, but the former is 20% cheaper.

Table 3. The Effect of Calcium Carbonate Content on the Tensile Strength of Filled Polypropylene

Calcium carbonate content (400 mesh)	0%	10%	20%	30%
Tensile strength (kg/cm^2)	183.9	80.9	73.6	58.9

We have also studied the effect of using mixtures of fly ash and calcium carbonate on the tensile strength of filled polypropylene. It was found that such mixtures are better than using calcium carbonate alone, but not as good as using fly ash alone. Also, the more fly ash present in such mixtures, the greater the tensile strength of the product is.

The resistance of polypropylene, filled with varying amounts of fly ash, to common chemicals was also studied. The resistance to common organic solvents is very good (weight change $<5\%$) to excellent (weight change $<1.5\%$); the resistance to xylene and chloroform is even better than pure polypropylene. The resistance to alkaline solutions is also excellent, with the exception of resistance to concentrated ammonia where the weight change is still less than 5%. The resistance to concentrated strong acids is not very good (weight change 5–10%), but the resistance to dilute solutions of strong acids ($\sim 10\%$) is excellent to very good. Polypropylene

filled with calcium carbonate showed very similar resistance to chemicals as with fly ash.

The water absorptivity of polypropylene filled with 10–30% of fly ash is below 0.05% as determined by immersing samples in water for seven days. Thus, fly ash filled polypropylene has a tensile strength, chemical resistance and water absorptivity similar to pure polypropylene, but of course the fly ash filled product is cheaper and can also solve the problem of disposing of large quantities of fly ash generated from burning coal. Finally, the color of fly ash filled polypropylene can be changed from black to silver-white or to violet by adding small amounts of titanium oxide or iron oxide. Other colors can be produced by adjusting the amount and the kind of pigments added. This has increased the utilization of commercial uses of fly ash filled polypropylene.

B. Urea-Formaldehyde Resin Filled with Fly Ash

Urea-formaldehyde resin filled with 20% of fly ash was compression molded to give a sample which showed a tensile strength of 165.6 kg/cm^2 and an impact strength (Izod notched) of 0.23 ft-lb/in. These results are inferior to those using α-cellulose as the filler. The water absorptivity of a fly ash filled sample was 13.4% as compared to 0.6% obtained with α-cellulose. The resistance to organic chemicals is excellent, but the resistance to acids and bases is poor for both the fly ash and α-cellulose filled urea-formaldehyde resins.

CONCLUSIONS

Polypropylene filled with 20–30% by weight of fly ash can be compression molded to give a product which shows good tensile strength and resistance to common chemicals and water. Pigments can also be added to give products of different colors. These properties are better than those obtained with the conventional filler calcium carbonate. The costs of making polypropylene goods are thus lowered. On the other hand, urea-formaldehyde resin filled with 20% by weight of fly ash is inferior to the one filled with

α-cellulose and thus can only be used for lower grade products.

It is seen from this study that fly ash can be used effectively as a filler for polypropylene. It points out a possible way of disposing large quantities of fly ash generated from thermopower plants. Whether fly ash can be added to other commodity polymers will be further examined.

ACKNOWLEDGEMENT

Financial support of this research by the Taiwan Power Co. is gratefully acknowledged.

REFERENCES

(1) T. Fukunaga, N. Kyohisa and K. Shimizu, *Jap. Kokai Tokyo Koho*, 79, 141, 818, Nov. 5, 1979.
(2) Symposium of Fly Ash Utilization, *United States Bureau of Mines Information Circular* 8640, 1973.
(3) (a) R. L. Kaas, *Plast. Des. Process*, 18, 49 (1978).
(b) R. L. Kaas, *Plast. Eng. Tech. Pap.*, 24, 266 (1978).
(4) W. S. Underwood and L. Bohn, *U. S.* 4, 301, 060, Nov. 17, 1981.
(5) L. C. Ehrenreich, H. S. Katz and J. V. Milewski, *Proc. Annu. Conf. Reinf. Plast./Compos. Inst., Soc. Plast. Ind.*, 33, Sec. 2-A, 1 (1978).
(6) H. T. O'Donnell, *U. S.* 4, 147, 687, Apr. 3, 1979.

If the past has taught us anything, it is that every cause brings its effect, every action has a consequence. This thought, in my opinion, is the *moral foundation* of the universe; it applies equally in this world and the next.

We Chinese have a saying: "If a man plants melons, he will reap melons; if he sows beans, he will reap beans." And this is true of every man's life: good begets good, and evil leads to evil.

True enough, the sun shines on the saint and the sinner alike, and too often it seems that the wicked wax and prosper. But we can say with certitude that, with the individual as with the nation, the flourishing of the wicked is an illusion, for, unceasingly, life keeps books on us all.

In the end, we are all the sum total of our actions. *Character* cannot be counterfeited, nor can it be put on and cast off as if it were a garment to meet the whim of the moment. Like the markings on wood which are ingrained in the very heart of the tree, character requires time and nurture for growth and development.

MAYLING SOONG
宋 美 齡

UV CURABLE HYBRID SYSTEMS OF EPOXY RESINS AND EPOXY ACRYLATE RESINS

JONQ-MIN LIU and SHAW-JI SHIAU

1. INTRODUCTION

UV curing has emerged as a rapidly growing method for the fabrication of essentially polution-free coatings, having only a fraction of the energy requirements of traditional thermally cured materials.[1] While the bulk of the work in UV curing to date has involved the radical polymerization of vinyl compounds,[2] during the past eight years discovery of several new photoinitiator compounds now make it possible to effect the UV-cure of epoxy resins by a cationic process.[3-5]

Even with the most reactive cationically-polymerizing epoxy systems, cure speeds still fall short of those obtainable with acrylic/free radical photoinitiator combinations. However, an important compensating feature of the epoxy/cationic photoinitiator system is that many of the properties that are obtainable are superior, such as adhesion to metallic substrates, etc.[6] In addition, oxygen inhibition of surface cure is not a problem with cationically-curable systems.[7] Interest is currently being shown in 'hybrid' systems combining both acrylic and cationic polymerization principles. The advantages of both types may to some extent be obtained. In this article, the studies of a hybrid system, composed of epoxy resin and epoxy acrylate resin, are reported.

2. EXPERIMENTAL

A. Materials

a. Epoxy Resin

A liquid bisphenol A-epichlorohydrin epoxy resin is employed in this work. The resin is a commercial product of Shell Chemical Co. with the trade name of Epon-828.

b. Epoxy Acrylate Resin[8]

A reaction vessel equipped with a condenser, stirrer, nitrogen inlet and thermometer is charged with 70 g Epon-828, 28 g acrylic acid, 100 ml toluene, and 0.5 g tetramethylammonium chloride. The reaction mixture is maintained at 110°C and refluxed for about five hours until the reaction of epoxy groups is essentially complete as measured by a product acid number of less than ten. The solvent is removed under vacuum and the epoxy acrylate resin is recovered in a form of a viscous liquid.

c. Cationic Photoinitiator-Triphenyl Sulfonium Hexafluorophosphate in complex form with di-*n*-butyl orthophthalate.[9] A solution of 28.3 parts of $Ph_3S^+Cl^-$ in 28.3 parts of water is added to a solution of 17.8 parts of KPF_6 in 65.9 parts of water and 35.1 parts of di-*n*-butyl orthophthalate. The organic phase is then separated and washed twice with 116.4 parts of deionized water and then dried by heating to about 60°C at 20 torr to remove traces of water.

d. Radical Photoinitiator-Benzoin Isopropyl Ether. The compound is purchased from Aldrich Chemical Co. and used without further purification.

B. Compounding

		parts by weight
Resin A:	Epon-828	100
	$Ph_3S^+PE_6^-/C_6H_4(COOC_4H_9)_2$	5
Resin B:	Epoxy Acrylate	100
	Benzoin Isopropyl Ether	3

	Resin A(% Wt.)	Resin B(% Wt.)
Resin-1	100	0
Resin-2	80	20
Resin-3	50	50
Resin-4	20	80
Resin-5	0	100

C. Instruments

a. Curing: Model UV C-101, C-Sun Industrial Co. Ltd. The machine is equipped with a medium pressure mercury lamp of 80 W per centimeter and a conveyor of adjustable speed.
b. Flexibility Test: Cylindrical Mandrel Bending Tester, Model 266, Erichsen Co.
c. Adhesion Test: Cross Hatch Cutter, Model 295, Erichsen Co.
d. Hardness: Hardness Rocker, Sward Type, Sheen Co.
e. Impact Resistance: Variable Impact Tester, custom-made.
e. Impact Resistance: Variable Impact Tester, custom-made.
f. The testing panels are made of tin plates.

3. SCREENING AND TESTING OF HYBRID RESINS

The curing rates of hybrid systems are measured by the number of passes of coated panels through the UV curing machine with a fixed conveyor speed. The results are shown in Table 1. The curing rate increases with the content of acrylate resin.

Table 1. Curing Speed of Hybrid Resins

	Resin-1	Resin-2	Resin-3	Resin-4	Resin-5
6.24 m/min	5	4	1	1	1
4.99 m/min	3	3	1	1	1
3.75 m/min	3	2	1	1	1
2.14 m/min	1	1	1	1	1

The flexibility of cured films is measured by the bending test. The results are shown in Table 2. The best flexibility belongs to the hybridized resin of a one to one weight ratio of epoxy and epoxy acrylate.

Table 2. Bending Test of UV Cured Hybrid Systems

	Resin-1	Resin-2	Resin-3	Resin-4	Resin-5
Run 1.	19 mm	6 mm	2 mm	25 mm	32 mm
Run 2.	19 mm	19 mm	2 mm	19 mm	32 mm

Evaluation of adhesive strength between coating material and the metallic substrate by the Grid Cutting Test is shown in Table 3. The adhesive strength increases with the content of epoxy resin.

Table 3. Adhesion of UV Cured Hybrid Systems

	Resin-1	Resin-2	Resin-3	Resin-4	Resin-5
Run 1.	***	***	***	**	*
Run 2.	***	***	***	**	*
Run 3.	***	***	***	**	*
Run 4.	***	***	**	*	*
Run 5.	***	***	***	**	*

***good, **medium, *bad

The impact resistance is determined with a Drop-Ball Impact Tester. The best impact resistance is obtained with the hybrid resin of a one to one ratio (Table 4).

Table 4. Impact Resistance of UV Cured Hybrid Systems

	Resin-1	Resin-2	Resin-3	Resin-4	Resin-5
Run 1.	25,000 gcm	50,000 gcm	50,000 gcm	10,000 gcm	5,000 gcm
Run 2.	15,000 gcm	15,000 gcm	50,000 gcm	20,000 gcm	10,000 gcm
Run 3.	15,000 gcm	35,000 gcm	50,000 gcm	25,000 gcm	12,500 gcm

The hardness of cured films is measured by counting the number of oscillations of a Sward type Rocker on the test panel. The results are expressed as percentage of number of oscillations made on a glass-plate standard which represents 100/100. There is no obvious correlation between the hardness and hybridizing ratio (Table 5).

Table 5. Rocker Hardness of UV Cured Hybrid Systems

Resin-1	Resin-2	Resin-3	Resin-4	Resin-5
26/100	18/100	16/100	22/100	20/100

4. CONCLUSION

According to the testing results, the following conclusions can be deduced: (A) With the mixing ratio of epoxy and epoxy acrylate being one to one, the hybrid system exhibits high curing speed, excellent impact resistance, excellent flexibility, good adhesion and fair hardness. (B) With the ratio being one to four or four to one, the hybrid systems exhibit properties very similar to those of the major component, i.e., neat epoxy resin or neat epoxy acrylate resin.

REFERENCES

(1) J. Pelgrims, *J. Oil Col. Chem. Assoc.*, **61**, 114 (1978).
(2) G. Berner, R. Kirchmayr and G. Rist, ibid, **61**, 105 (1978).
(3) W. Watt, *U.S. Patents*, 3, 794, 576 (1974).
(4) J. Crivello and J. Lam, *Macromolecules*, **10**, 1307 (1977).
(5) J. Crivello, *U.S. Patents*, 4,058,400 and 4,058,401 (1977).
(6) E. Irving and B. Stark, *Brit. Polym. Jr.*, **15**, 24 (1983).
(7) R. Nickerson, Sr, *Industrial Finishing*, p. 10 (Feb. 1974).
(8) F. Fekete, *U.S. Patents*, 3,373,075 (1968).
(9) R. Carlson, *U.S. Patents*, 4,231,886 (1980).

It is not enough that you should understand about applied science in order that your work may increase man's blessings. *Concern for man himself and his fate must always form the chief interest of all technical endeavours...* in order that the creations of our mind shall be a blessing and not a curse to mankind. Never forget this in the midst of your diagrams and equations.

ALBERT EINSTEIN

When you sit with a nice girl for two hours you think it's only a minute. But when you sit on a hot stove for a minute you think it's two hours. That's *relativity.*

ALBERT EINSTEIN

THE STRUCTURE OF GONAD OF THE TOPMINNOW, *GAMBUSIA PATRULIS*

CHUNG-HSIUNG WANG

ABSTRACT

The topminnow, *Gambusia patrulis*, is a ovoviviparous teleost. In order to understand the relationship between gonopodium and sex, a detailed histological study of the structure of the gonad of this species was made. The results reveal that all male fish posses gonopodia but fish possessing gonopodia may be male, female or hermaphrodite. The natural hermaphroditism of topminnow was also reported in this paper.

INTRODUCTION

The topminnow, *Gambusia patrulis*, is a common fresh water fish in Taiwan. It belongs to order Cyprinodontiformes[9]. Many papers and reviews regard the subject of sex determination, gonad structure and sexual reversal induced artificially of Cyprinodontiformes, but there are few studies about the natural hermaphroditism of these fishes[1,12,15,16]. This paper describes the general histology of the gonad and the hermaphroditic phenomenon of *G. patrulis*.

MATERIALS AND METHODS

The topminnow, *Gambusia patrulis*, employed in the present investigation were netted in the drain surrounding Fu-Jen University. The gonads of 107 specimens were prepared for histological observation. The gonads were fixed in either Bouin or Susa fixatives and embedded in paraffin and sectioned at 7 μm. Sections of all gonads were stained with Delafield hematoxylin and eosin Y, and examined with a bright field compound microscope.

OBSERVATIONS AND DISCUSSIONS

I. The gonopodium of topminnow

Gambusia patrulis has internal fertilization. The copulatory

organ of topminnow is a specialized anal fin referred to as the "Gonopodium". It is modified through the elongation and specialization of 3rd, 4th and 5th of its rays. It is reported that during sexual activity the elongated bony fin rays and the web of tissue connecting these rays interact to form a transitory groove presumably associated with the transfer of sperm bundles to the tip of the gonopodium[9].

In the past time, we used to distinguish the male from the female fish by the possession of the gonopodium. In the present histological study on the gonads of these fish, it can be shown that all male fish have gonopodia but the fish possessing gonopodia may be male, female or hermaphroditic. Here we should mention that many fish possess the intermediate type of the anal fin (Fig. 1). Consequently we suggest that the reversal of sex may occur in topminnow.

II. The histology of the gonads

(a) *The ovary* (Fig. 2)

The ovary of topminnow is a single sac-like organ on the median-dorsal position to the coils of the intestine. It is supported dorsally by a connective tissue forming the mesovarian. The ovary is surrounded by a pigmented membrane, usually the ovary of young fish is white in color, but the mature ovary is yellowish because it has many fully developed ova containing large amounts of yolk. At the posterior end of the ovary is a short oviduct which leads to the genital opening at the base of the anal fin. It is better to use the young fish to observe the general histology of the ovary, since vitellogenesis and subsequent embryo development markedly alter the basic structure of the ovary. A transverse section of the ovary of a young fish is shown in Fig. 2. The outer surface is covered with a thin squamous peritoneal epithelium. Within the epithelium lies a thin layer of mesenchymal connective tissue. The inner border of the ovarian wall is lined by a layer of pseudostriatified columnar cells. The ovarian lumen lies along the dorsal side of the ovary. The ovarian wall forms some ovigerous folds. In a fully developed

ovary, these folds obliterate the ovarian lumen. It is filled with many ova of various stages between the inner and outer border of the ovarian wall. The oogonial nests are located near the inner epithelial layer. As the oocytes develop further they move progressively away from the oogonial nest to the outer part of the ovarian wall. The oocyte is surrounded by a layer of small epithelial cells to form an ovarian follicle. In the spawning season, the sperms which come from the male fish can be found in the ovarian lumen and ovarian epithelium. The fully developed oocytes are fertilized by those sperms stored in the ovary. The fertilized ova are still in the follicle. The follicle acts as the site of development of fertilized ova to a very advanced embryo stage. When the embryos are fully developed, these young fish are discharged from the ovarian follicle to the ovarian cavity.

(b) *The testis* (Fig. 3)

The testis of topminnow is a single bilobed organ on the roof of the abdominal cavity, ventral to the airbladder and dorsal to the coil of the intestine. This white organ is kept in place with the membraneous mesoarchium. A thin pigmented membrane envelops the entire testis. A single sperm duct emerges from the posterior end of the testis to the urogenital opening at the base of the gonopodium. A transverse section of the testis is shown in Fig. 3. The visceral peritonium of the testis is a simple squamous epithelium. A thin layer of connective tissue lies beneath the epithelium. The testis of topminnow is of an acinar type. Each lobe of the testis has one main sperm duct which runs along the axis of the body. These two ducts fuse together posterior to form a vas deferens. The main sperm duct gives rise to some short ducts (vas efferentia). They are arranged perpendicular to the main sperm duct. These tubules do not penetrate to the periphery of the organ but to a very short distance away from the main sperm duct. Scattered germ cells appear near the periphery of the testis. Spermatogonia proliferate from these testis germ cells to form a cyst which is surrounded by a layer of cells. All cells within one cyst are

in the same stage of development. The cysts undergo various stages of maturation as they are moving toward the sperm duct. In spermatophores, the sperms are aggregated and arranged with their tails directed centrally and the head oriented peripherally to form the sperm balls. The sperm balls may receive a gelatinous secretion which binds them together so that they remain intact during transfer to the female[9]. When mature spermatophores reach the efferent ducts, the epithelial cells of the cyst become confluent with the epithelial cells of efferent ducts and discharge their contents.

(c) *The ovotestis* (Fig. 4)

The external structure of the ovotestis is like that of the typical ovary. A cross section of an ovotestis is shown in Fig. 4. The internal structure of the ovotestis differs from both testis and ovary. Some ovotestes contain embryos in one side and testicular tissue with some ova in the another side. Generally, the ovarian tissue is not separated from the testicular tissue. The cysts of male germ cells grow into the degenerating ovarian tissue. Cysts seem to have no regular arrangement as in the typical testis. Various stages of spermatogenesis can be observed. Well-developed spermatozoa are found in the ovotestis. The ova are in various stages but none of them is mature.

The sex reversal is common in teleosts. It occures naturally and can be induced artificially[2,8,10,11,13,14]. Ovotestes have been produced artificially by means of sex hormone treatment of *G. affinis*[16]. But a natural hermaphrodite in the genus *Gambusia* has never been reported. It seems that the ovotestis of topminnow is a temporary stage. The phenomenon of sex reversal remains to be elucidated.

REFERENCES

(1) Ats, W. J. *Intersexuality in fish.* In "Intersexuality in Vertebrates including Man". 145-232. Eds. C. N. Armstrong and A. J. Marshall. Academic Press, N. Y. (1966).

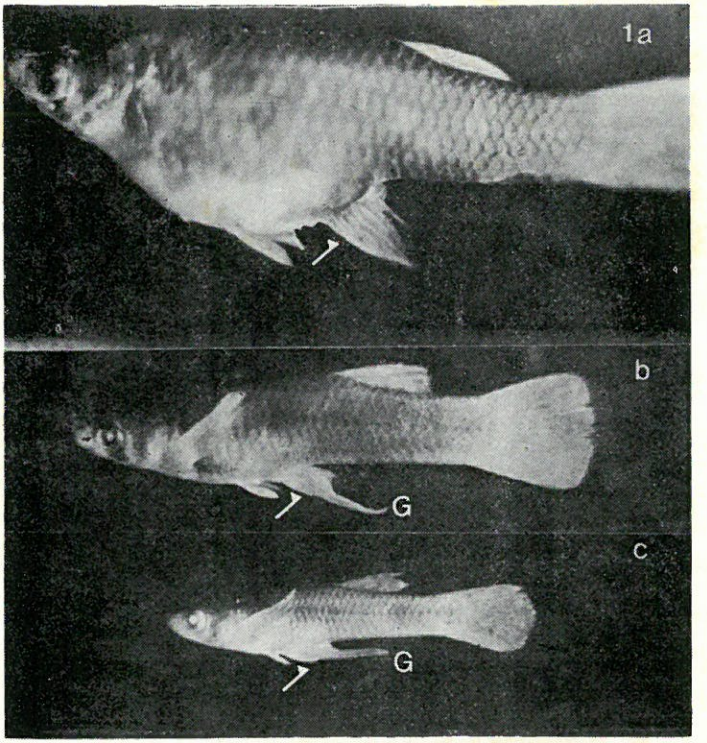

Fig. 1. Photographs of Gambusia partulis showing the differences in shape of anal fin (arrows) of female (a), hermaphroditic (b) and male (c) fish. G: gonapodium.

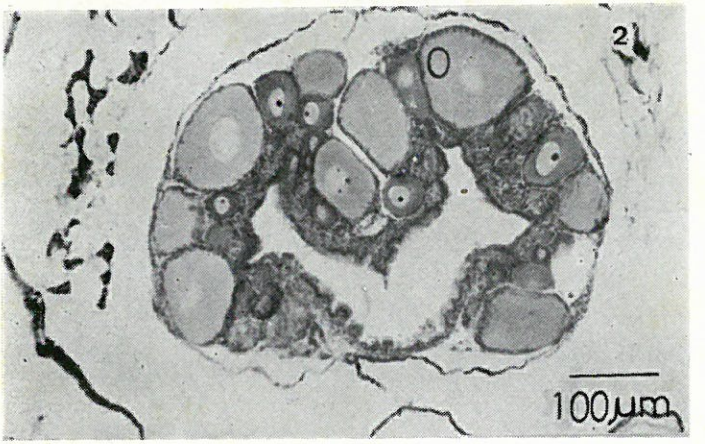

Fig. 2. Micrograph of the histological section of the ovary. O: oocyte.

Fig. 3. Micrograph of the histological section of the testis. S: sperm.

Fig. 4. Micrograph of the histological section of the ovotestis. O: oocyte, S: sperm.

(2) Brusle, S. Contribution to the sexuality of a hermaphroditic teleost, *Serranus hepatus*. *J. Fish Biol.* 22(3), 283-292, (1983).
(2) Chan, S. T. H. and J. G. Phillips. The structure of the gonad during natural sex reversal in *Monopterus albus* (Pisces: Teleostei). *J. Zool., Lond.* **151**, 129-141, (1967).
(4) Chang, K. H. and S. Chen. The age and growth of red sea bream in Pescadores Island. *Bull. Iast. Zool., Academia Sinica* **11**, 11-19, (1972).
(5) Chung-Chia Huang, Chu-Fang Lo and Kun-Hsiung Chang. Sex reversal in one sparid fish, *Chrysophrys major* (Perciformes, Sparidae). *Bull. Inst. Zool., Academica Sinica* **13**(2), 55-60, (1974).
(6) Coetzee, P. S. Seasonal histological and macroscopic changes in the gonads of *Cheimerius nufar* (Sparidae: Pisces). *S. AFR J. Zool.* **18**(2), 76-88, (1983).
(7) Etessami, S. Hermaphroditism in 1 Sparidae of the Persian Gulf: *Acanthopagrus bifasciatus*. *Cybium*, **7**(2), 87-90, (1983).
(8) Fujii, T. Hermaphroditism and sex reversal in the fishes of the Platycephalidae-1. Sex reversal of *Onigocia macrolepis* (Bleeker). *Jap. J. Ichtyol.* **17**(1), 14-20, (1970).
(9) Hoar, W. S. Reproduction. In "Fish Physiology" 1-59. Eds. Hoar, W. S. and Randall, D. J. Academic Press N. Y. (1969).
(10) Hoffman, S. G. Sex-related foraging behavior in sexually hermaphroditic hogfish (Bodianus spp). Ecology, **64**(4), 798-808, (1983).
(11) Moser, H. G. Seasonal histological changes in the gonads of *Sebastodes paucispinis* Ayres, an ovoviviparous teleost (Family Scorpaenidae). J. Morph. **123**, 329-354, (1967).
(12) Reinboth, R. Intersexuality in fishes. In "Hormones and Environment". Eds. G. K. Benson and J. G. Phillips. Men. Soc. Endocrinol. **18**, 515-543, (1971).
(13) Robertson, D. R. Social control of sex reversal in a coral-reef fish. Science **177**, 1007-1009, (1972).
(14) Schenck, J. R. and B. G. Whiteside. Reproduction, fecundity, sexual dimorphism and sex ratio of *Etneostoma fonticola* (Osteichthyes: Percidae). A. M. MIDL. NAT. **98**(2), 365-375, (1977).
(15) Yamamoto, T. O. A further study on induction of functional sex reversal in genotypic males of the medaka (*Oryzias latipes*) and progenies of sex reversals. Genetics, **44**, 739-757 (1959).
(16) Yamamoto, T. O. Sex differentiation. In "Fish Physiology" V. 3, 117-175. Eds. W. S. Hoar and D. J. Randall. Academic Press, N. Y. (1969).

There are *verities,* and they are still *eternal.* In spite of every change and through every change that is now taking place and will take place in the unimaginable future, the verities remain unchanged.

It is a wonderful fact that while the peoples of the earth differ much in the ways in which they think, yet upon what is good and evil they all agree. A good man in any country is the same man. He is the honest man, the man who thinks of others when he thinks of himself, the man whom people can trust for magnanimity as well as for justice. This is eternal verity.

PEARL S. BUCK

WATER PERMEABILITY OF DORMANT AND NON-DORMANT RICE SEEDS DURING GERMINATION

BAO-WEI P. LIU

INTRODUCTION

A number of studies have discussed the mechanism of rice-seed dormancy. Takahahi[6] demonstrated that the embryo and its endosperm but not the hulls were the main factor to control the seed dormancy in a wild variety of rice. Mikkelson and Sinah[5] found a water soluble inhibitor in the hulls of *Oryza sativa*, japonica var., which was able to prevent the germination of seeds. Kato *et al.*[2] also found organic inhibitors in the seed coat of rice which could inhibit seed germination and growth of seedlings. On the other hand, Chu and Kao[1] emphasized peroxidase activity in the hulls of dormant varieties. Therefore, different machanisms to control the germination of seeds exist in various varieties of rice.

In the dormant variety of Taiwan wild rice, designed P-10, Wu[8] suggested that the prevention of water permeability by the hulls and seed coat was the factor to control seed germination. However, Liu and Huber[4] gave a different conclusion when they studied the DNA synthesis in the embryo of P-10 seed during imbibition. To determine whether there is an effect of water absorption on germination of P-10 seeds was the topic of this research. In addition, the relationship between water absorption during imbibition and germination among various varieties of rice was also included in this study.

MATERIAL AND METHOD

Seeds of one of the dormant Taiwan wild rice family designated P-10 were propagated in the greenhouse on campus of Fu Jen

* This work was supported by the National Science Council, Republic of China grant NSC 72B-0409-030-01.

University. Rice seeds of other varieties used in this experiment were obtained from the Taiwan Provincial Agriculture Experiment Station. Except P-10 seeds all other varieties in this experiment possessed non-dormant characteristics. P-10 seeds were able to germinate normally when the hulls were removed. The water absorption capacity in sequent periods during imbibition was conducted on both hulled and unhulled seeds of each variety. Hulled seeds were imbibited in radioactive ^3H_2O after the hull had been removed whereas unhulled seeds were imbibited with intact seeds. All seeds were imbibited on filter paper with 5 ml of ^3H_2O at a concentration of 1 μCi ^3H_2O/ml H_2O in a petri dish within the growth incubator maintained at 25°C±1. From the beginning of imbibition to the commencement of germination in each treatment, at 6 hour intervals during imbibition, the whole or part of a seed (embryo or endosperm) was crushed to powder with a pastle and mortor and then removed into a vial added with 1.5 ml protosol. After 2 hours of digestion with protosol at 55°C, each sample was mixed with 9 ml of cocktail solution (2.5 gm PPO and 0.025 gm POPOP dissolved in 1 liter toluene) evenly and counted with Beckman Liquid Scintillation Counter.[3] Each treatment was replicated three times.

According to the average radioactivity count per minute (cpm) in each treatment, the actual quantity of absorption per weight of tissue was obtained from the following caculation:

The reading was 3363 cpm in the standard sample which contained 0.002 μCi of ^3H_2O in prepared seed tissue after imbibition in cool solution. In this case, 1,681,500 cpm should be derived if 1 μCi of radioactivity was in the sample. Since all seeds were imbibited in a radioactive concentration of 1 μCi/ml, the actual ml of water absorption per gm of tissue is defined by A: where

$$A = \frac{\text{cpm} - \text{background counting}}{\text{weight of tissue in gm} \times 1{,}681{,}500 \text{ cpm}}.$$

RESULTS AND DISCUSSIONS

Hulled seeds of both dormant P-10 and non-dormant Taichung-65 were able to germinate within a 24 hour period during imbibition.

On the other hand, seeds of Taichung-65 with hull were able to germinate within 30 hours of imbibition but seeds of P-10 with hull were unable to germinate even after 5 days of imbibition. A comparison was made in the water absorption of whole seeds during imbibition among Taichung-65 and P-10 hulled seeds, Taichung-65 and P-10 unhulled seeds. (Fig. 1) The rates of water absorption in the hulled seeds of both P-10 and Taichung-65 which might correlate with their respective rates of germination were faster than that of seeds with hulls. There were no major differences between the water absorption of unhulled seeds of P-10 and Taichung-65 during imbibition. Therefore the inhibition of water permeability of hull is not the limiting factor to cause the dormancy of P-10 seeds. This result disagreed with Wu's prediction[8] who believed that hulls of P-10 were less permeable than the hulls of non-dormant seeds. The water absorption of endosperm during imbibition among the same

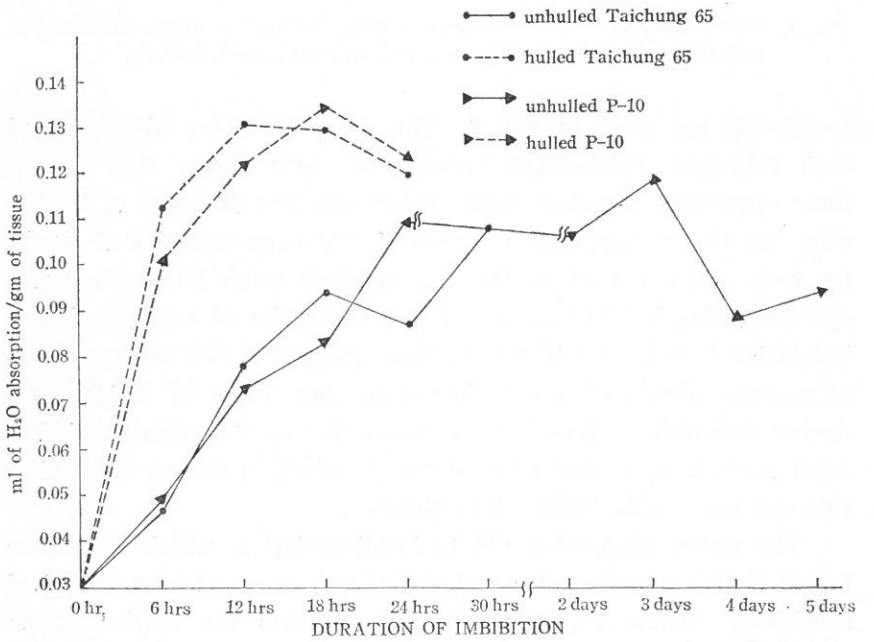

Fig. 1. Water absorption of whole seeds during imbibition among Taichung-65 and P-10 hulled seeds, Taichung-65 and P-10 unhulled seeds.

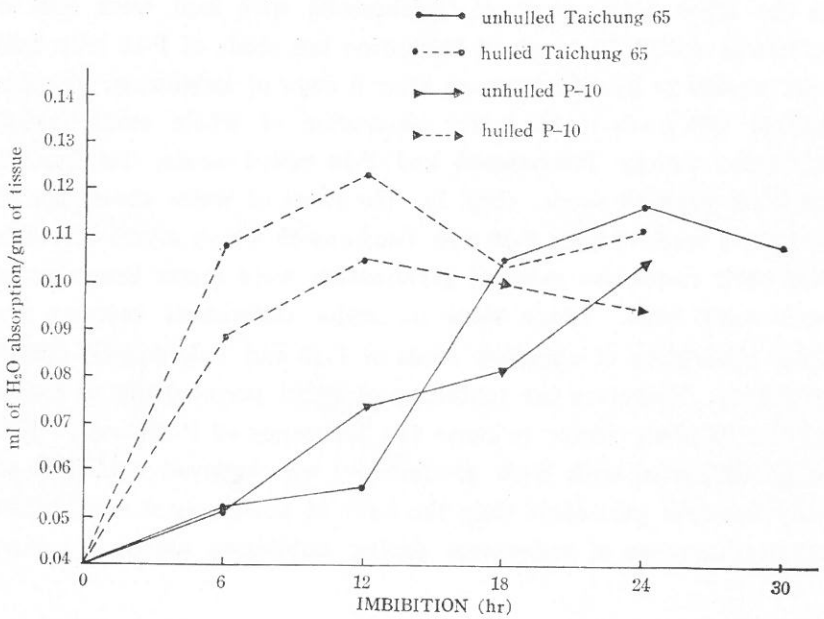

Fig. 2. Water absorption of endosperms during imbibition among Taichung-65 and P-10 hulled seeds, Taichung-65 and P-10 unhulled seeds.

treatments are given in Fig. 2. The ability of water absorption of both P-10 and Taichung-65 hulled seeds was higher than that of their respective unhulled seeds before the first 18 hours of imbibition. By the comparison of unhulled Taichung-65 and P-10 seeds, the hulls did not prevent the movement of water into endosperms of P-10 during imbibition. The water absorption of embryos during imbibition is indicated in Fig. 3. The embryos of P-10 always showed a lower ability of water absorption than those of Taichung-65 during imbibition. Whether the lower degree of hydration of dormant P-10 embryos might arrest the germination during imbibition, this question needs further investigation.

The water absorption ability in all varieties, which have been tested in this experiment, reached the peak at an 18 hour period of imbibition (Table 1). These results confirm the earlier water absorption results reported by Takahahi.[6] In addition, hulled seeds in all varieties exhibited a much higher water absorption

Table 1. Average milliliter of water absorption of grain per gram of tissue during imbibition among hulled and unhulled seeds of different varieties. Each value represents the mean of 3 replications and it's standard deviation

Treatment \ Duration of imbibition		6 hrs	12 hrs	13 hrs	24 hrs	30 hrs
Leou Tour Tzyy	unhulled	0.0743±0.0140	0.1022±0.0196	0.1269±0.0139	*0.1122±0.0059	0.1144±0.0028
	hulled	0.1218±0.0114	0.1368±0.0126	*0.1282±0.0092	0.1269±0.0135	
San ShyTzyy	unhulled	0.0593±0.0155	0.0949±0.0085	0.1024±0.0174	0.1071±0.0103	*0.1094±0.0030
	hulled	0.1160±0.0072	0.1038±0.0137	*0.1358±0.0137	0.1225±0.0265	
I-Tam-Lun	unhulled	0.0658±0.0153	0.0803±0.0109	0.1087±0.0168	0.0847±0.0200	*0.1043±0.0039
	hulled	0.1008±0.0081	0.1246±0.0139	0.1220±0.0100	*0.1244±0.0059	
Dah LihChing You	unhulled	0.0778±0.0192	0.0898±0.0164	0.0944±0.0177	*0.1011±0.0227	0.1198±0.0066
	hulled	0.0953±0.0254	0.1156±0.0254	*0.1379±0.0077	0.1333±0.0055	
Kariiranga	unhulled	0.0448±0.0073	0.0880±0.0059	0.0978±0.0150	0.1074±0.0108	*0.1089±0.0058
	hulled	0.1115±0.0184	0.1340±0.0038	0.1320±0.0047	*0.1367±0.0175	
Taichung 65	unhulled	0.0473±0.0021	0.0788±0.0231	0.0945±0.0124	0.0878±0.0223	*0.1088±0.0100
	hulled	0.1121±0.0098	0.1308±0.0157	0.1300±0.0091	*0.1205±0.0230	

* Most of the seeds (85%) in this lot germinated at that time.

capacity in the first 6 hours of imbibition than unhulled seeds in their respective varieties. In the same variety, hulled seeds usually germinated 6 hours earlier than unhulled seeds. Therefore, the delay of germination of unhulled seeds might be due to the hulls which prevented the water absorption of seeds in the early inhibition stage.

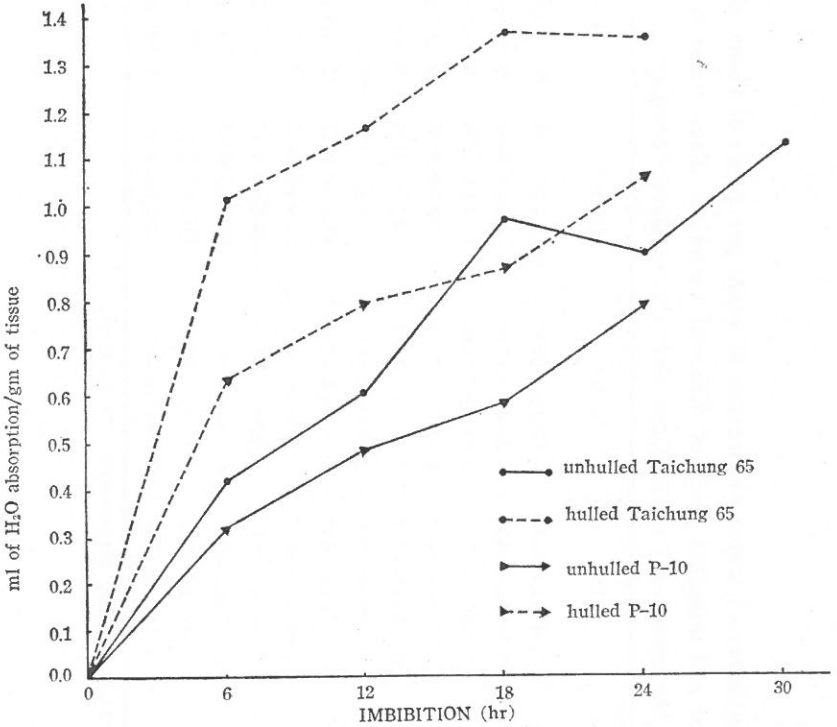

Fig. 3. Water absorption of embryos during imbibition among Taichung-65 and P-10 hulled seeds, Taichung-65 and P-10 unhulled seeds.

REFERENCES

(1) Chu, C. and W. H. J. Kao. Physiological studies germination and dormancy of Rice (*Orysa sativa*) seeds. *Nat. Sci. Coun. Mont.* **6**, 1034-54, (1978).

(2) Kate, T., M. Tsunakawa, N. Sasak, H. Aizawa, K. Fujita, Y. Kitahara, and N. Takahashi. Growth and germination inhibitors in rice husks. *Phytochem.* **16**, 45-48, (1977).

(3) Kobayashi, Y. and D. Maudsloy. *Biological applications of Liquid scintillation counter.* Acad. Press. pp. 152-169, (1974).
(4) Liu, P. B. W. and F. Huber. Nuclear DNA content in meristematic cells of dormant and germinating embryos of rice seeds. *Bot. Bull. Acad. Sinica.* **21**, 15-23, (1980).
(5) Miskkelson, D. S. and M. N. Sinah. Germination inhibition in *Oryza sativa* and control by preplanting soaking treatment. *Crop Sci.* **1**, 322-3, (1963).
(6) Takahahi, N. Studies on dormancy of wild rice seeds II. Roles of seed coat, embryo and endosperm in dormant seeds. *Rep. Inst. Agr. Res. Tohoku Univ.* **14**, 75-85, (1963).
(7) Takahahi, N. The relation of water absorption to germination of rice seeds. *Rep. Inst. Agr. Res. Tohoku Univ.* **12**, 61-72, (1961).
(8) Wu, L. The seed dormancy of a Taiwan wild rice population and its potential for rice breeding. *Bot. Bull. Acad. Sinica* **19**, 1-12, (1978).

The idea of what is *true merit* should often be presented to youth, explained and impressed on their minds, as consisting in an inclination joined with an ability to serve mankind, one's country, friends and family; which ability is to be acquired or greatly increased by true learning; and should indeed be the great aim and end of all learning. I think that nothing is of more importance for the public weal, than to form and train up youth in wisdom and virtue.

Wise and *good* men are, in my opinion, the strength of a state far more so than riches or arms, which, under the management of ignorance and wickedness, often draw on destruction, instead of providing for the safety of the people. And though the *culture* bestowed on many should be successful only with a few, yet the influence of those few and the service in their power may be very great.

BENJAMIN FRANKLIN

CONTRIBUTORS TO THIS NUMBER

Ying-Sheng Huang 黃鶯聲, former graduate student in physics at Fu Jen University, presently associate professor of electronic engineering and technology at the National Taiwan Institute of Technology, Taipei.

Shang-Kai Lee 李尙鎧, lecturer in physics at Fu Jen University.

Frank E. Budenholzer, SVD, 柏殿宏, professor of chemistry and director of the Graduate School of Chemistry at Fu Jen University.

Lin-Sheng Huang 黃霖生, graduate student in chemistry at Fu Jen University.

Shang-Shing P. Chou 周善行, associate professor of chemistry at Fu Jen University.

Chung-Bin Chu 朱宗彬, research assistant in the department of Chemistry at Fu Jen University.

Jonq-Min Liu 劉仲明, associate professor of chemistry at Fu Jen University.

Shaw-Ji Shiau 蕭紹基, research assistant in the department of Chemistry at Fu Jen University.

Chung-Hsiung Wang 王重雄, professor of biology and director of the Graduate School of Biology at Fu Jen University.

Bao-Wei P. Liu 劉寶瑋, professor of biology and chairman of the Department of Biology at Fu Jen University.

PRINTED BY

Ching Hua Press Co., LTD., Taipei